Design of a Mobile Binary Parallel Robot that Exploits Nonsingular Transitions

Adrián Peidró*, Alberto García-Martínez, José María Marín, Luis Payá, Arturo Gil, Óscar Reinoso

Automation, Robotics, and Computer Vision Laboratory
Miguel Hernández University, Avda. de la Universidad s/n, Elche 03202 (Spain)
**Corresponding author*
emails: apeidro@umh.es, alberto.garcia14@goumh.umh.es, jmarin@umh.es, lpaya@umh.es, arturo.gil@umh.es, o.reinoso@umh.es

Abstract

Sliding-frame mobile robots used for autonomously inspecting metallic structures consist of two bodies connected by few joints. They move by alternately adhering one body to the structure while moving the other body to the next position. Sliding-frame robots are simpler and offer safer adhesion than legged and wheeled robots, and their control can be simplified using binary actuators that adopt only two stable states. However, most existing sliding-frame robots require continuous actuators to reach targets with precision, since binary actuators impose steps of fixed length. To solve this, this paper presents a new sliding-frame robot consisting of two bodies connected through a 2RPR-PR kinematic chain driven by two binary actuators. The 2RPR-PR chain can perform nonsingular transitions, which is the ability of many parallel robots to switch between different poses corresponding to the same state of its actuators, without crossing singularities. Thanks to this, the poses reachable by the proposed robot are doubled, granting it a denser workspace and more accuracy than similar robots, using only two binary actuators. The feasibility of the proposed robot is shown through a prototype.

Keywords: Binary robot, Mobile robot, Parallel robot, Workspace, Singularities, Magnetic adhesion

1. Introduction

Climbing robots are necessary for performing inspection and maintenance tasks at heights in structures such as bridges, ship hulls, nuclear reactors, etc. Such tasks are dangerous for human operators since they imply risks like falling from height or exposure to toxic atmospheres or radiation. Climbing robots have been studied for decades. Dozens of models have been proposed and they can be classified depending on different criteria [1]. According to the technology they use for adhering to the climbed surface, they can be mainly divided in mechanical grasping, pneumatic suction, or magnetic adhesion, in addition to other less conventional experimental adhesion technologies. Depending on the locomotion mechanism, climbing robots can be mainly divided into legged robots, wheeled robots, sliding-frame robots, and wire-hanging robots.

Among the different locomotion types of climbing robots, sliding-frame robots have the advantages of mechanical simplicity and safer adhesion than other types, although they are slower [1]. Sliding-frame robots typically consist of two frames or bodies joined by few joints that provide from one to three relative Degrees of Freedom (DOF) between these bodies, allowing one body to slide with respect to the other. Each body has adhesive feet like magnets or suction cups, with which it can adhere firmly to the climbed surface. The locomotion of sliding-frame robots is illustrated in Figure 1. Initially, the first body is attached to the surface while the second one is free, then the second body is moved relative to the first one to a new position. Next, the second body is attached while the first one is freed, which allows moving the first body to a new position. Finally, the first body is attached and the second one is freed, starting again a new locomotion cycle.

As Figure 1 illustrates, there are two main topologies of sliding-frame robots. For the first topology shown in Figure 1a (Cartesian topology), the two bodies are connected by two orthogonal prismatic joints that enable it to change the position of one body with respect to the other, preserving the orientation of both bodies. Sometimes, a third auxiliary revolute joint is added between the bodies, only to correct small angular deviations that accumulate after some steps, to guarantee that the overall motion of the robot remains straight [2]. Examples of Cartesian sliding-frame robots are the SkyCleaners [3, 4] or the robots presented in [2, 5]. For the second topology shown in Figure 1b (polar topology), the two bodies are connected through a prismatic and a revolute joint, or a pin-in-slot joint, which allow one body to reach any position relative to the other in polar coordinates, with the possibility to use the revolute joint to adjust the final orientation of the robot after reaching the desired position, as illustrated in step 6 of Figure 1b (unlike Cartesian robots). Examples of polar sliding-frame robots are the MACS [6], the SADIE and NERO robots [7, 8], SURFY [9], Robicen [10], and the robot proposed in [11].

Some sliding-frame robots do not strictly follow the two main topologies of Figure 1. For example, the ANDI robot [12] and the robot proposed in [13] have three DOF connecting the two bodies, which allow the robot to reach any position and orientation with fewer steps than polar robots. Another example, the Planar Walker robot [14], is a quadrilateral whose sides

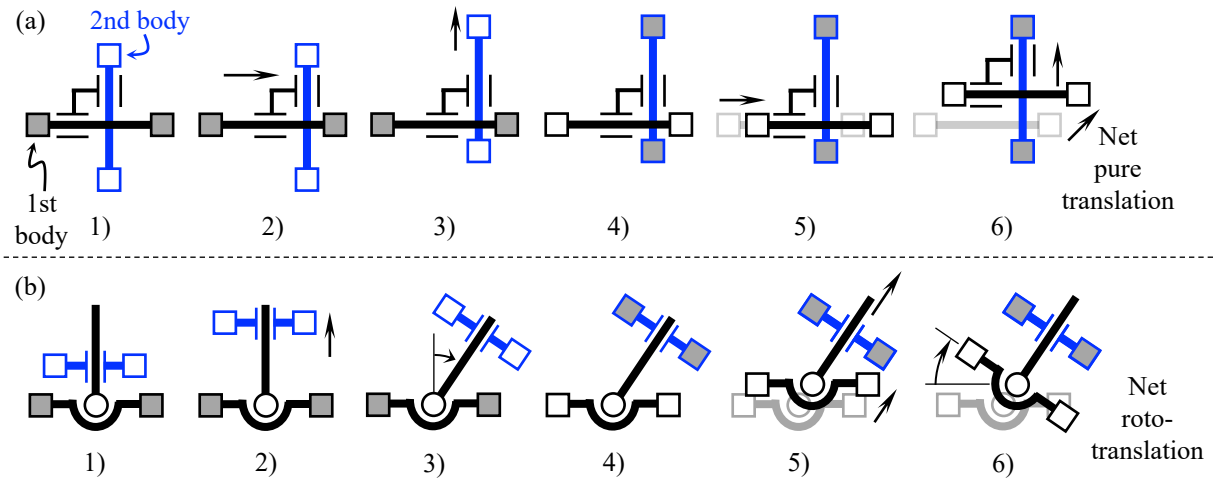

Figure 1: Inchworm-like locomotion sequence of (a) Cartesian sliding-frame robots, and (b) polar sliding-frame robots. Filled squares are feet attached to the ground. Empty squares are free feet.

are four pneumatic cylinders connected by revolute joints at four vertices, which are the feet. This robot walks by adhering two or three of the feet and extending or retracting the cylinders connected to the free feet, so that these can be attached to new positions. Unlike other sliding-frame robots, the pneumatic cylinders of the Planar Walker are binary, i.e., these are controlled in an on/off manner, completely extending or retracting them instead of performing a continuous feedback control to stop the cylinders at intermediate positions. Binary actuation greatly simplifies the control and path planning of sliding-frame robots, but it imposes a fixed step length and limits the precision of their movements, as only a discrete set of poses are reachable [9]. For this reason, most sliding-frame robots perform continuous position control of their actuators to reach the desired target with precision, but precise continuous control of pneumatic actuators (which are the most used actuators in sliding-frame robots) is very difficult due to nonlinearities [9, 15].

This paper presents a new polar sliding-frame mobile robot with binary actuators, intended for exploring metallic surfaces and climbing walls to perform inspection tasks with a camera. The robot consists of two bodies articulated through a pin-in-slot joint. Unlike most of the previous sliding-frame robots, which use a serially actuated kinematic chain between the two connected bodies, the proposed robot uses a parallel kinematic chain of the type 2RPR-PR[1], which connects these two bodies through three chains in parallel: a passive pin-in-slot joint and two crossed linear actuators. The proposed robot is called Xrobin, after X-shaped binary robot, and it effectively exploits the ability of many parallel mechanisms to perform what are known as *nonsingular transitions* (see [16] and references therein). These transitions allow the mechanism to switch between different postures corresponding to the same state of the actuators, without traversing singularities. The ability to perform nonsingular transitions can be used to widen the workspace of parallel robots, and it is a factor to be considered when designing them [17]. Thanks to this ability, the proposed sliding-frame robot can adopt eight different poses between the two connected bodies using binary actuators, which is twice the number of poses that one would typically expect from a robot with two binary actuators ($2^2 = 4$). By being able to reach eight different poses, the proposed robot has a very dense workspace that allows it to reach the desired target with high precision, even using binary actuators to simplify the control of the robot. This is not possible in previous sliding-frame robots, which typically use simpler yet more limited serial kinematic chains. Other previous robots need to be continuously actuated in order to reach targets with precision, because if they used binary actuation, they would reach only a sparser set of poses.

This paper is organized as follows. First, binary robots are reviewed in section 2. Next, section 3 describes the kinematics and gait of the proposed robot, explaining its ability to reach eight different poses using only two binary actuators, by exploiting nonsingular transitions. After that, section 4 presents the kinematic design of the robot, solving its polynomial equations to determine the dimensions required to reach the desired poses. In section 5, the workspace of the mobile robot is analyzed to demonstrate its high maneuverability despite having binary actuators, especially compared to the case in which the same robot does not exploit nonsingular transitions. Next, the development of a prototype is explained and demonstrated through experiments in section 6. Finally, section 7 summarizes the main conclusions and points out some lines of future work.

[1]Following the usual notation for parallel mechanisms, the following symbols will be used in this paper to denote different types of joints: R (revolute), P (prismatic), S (spherical). Underlined means actuated joint. Numbers indicate the number of times a kinematic chain is repeated. Dash (-) separates chains of different type. For example: the name of the "2RPR-PR" mechanism analyzed in this paper means that the base and platform of this mechanism are connected through three chains in parallel: two of type RPR (with actuated prismatic joint) and one of type PR.

2. Related Work: Binary Robots

Binary robots are driven by actuators that only adopt two stable states: ON/OFF, open/closed, 0/1, retracted/extended cylinder, etc. The main advantage of binary actuation in robotics is the lack or simplification of control, since it is only necessary to detect, at most, if the actuator reaches one of its extreme positions, without having to perform feedback control of the actuators throughout their continuous range of motion. This also simplifies trajectory planning and favors repeatability, since binary robots have discrete workspaces and can only reach the discrete poses contained in these workspaces [18].

However, due to the discrete nature of the workspace of binary robots, if finer precision is required, the robot must be provided with a sufficiently large number of binary actuators, which leads to *hyper-redundant manipulators* or *variable-geometry trusses* [19]. These hyper-redundant manipulators are built by stacking one binary module after another, constituting relatively long snake-like manipulators with so many reachable poses that their discrete workspaces look almost continuous. Typically, the individual modules that make up the global manipulator have a parallel or closed-loop kinematic structure, with each module consisting of two bodies (usually called "base" and "platform") interconnected through two or more serial kinematic chains placed in parallel, where some of these chains contain actuated joints. Modules with parallel kinematics are especially well-suited to build hyper-redundant binary manipulators due to their inherent rigidity, their high load-to-weight ratio [20], and the fact that many parallel manipulators are typically driven by cylinders, which can be easily actuated in a binary manner, by fully extending or retracting them.

Many examples of binary-actuated hyper-redundant manipulators or variable-geometry trusses can be found in the literature. For example, Chirikjian and co-workers [21, 22, 23], and Clysdale and Sun [24], analyzed planar manipulators made of several 3RPR planar parallel binary modules connected in series. To achieve three-dimensional motion, some 3RPR modules can be rotated by 90° with respect to the previous one [19], or specific discretely-actuated twist joints can be inserted between modules [25, 19]. Maeda and Konaka [26] and Tzorakoleftherakis et al. [27] studied hyper-redundant manipulators made of 3RPS parallel binary modules. Sometimes, a continuously-actuated robot is placed at the very end of these manipulators to achieve fine terminal positioning [20, 19]. Sujan and Dubowsky [28] designed a manipulator made of three-DOF parallel modules with flexure joints, for space applications. Other authors have built hyper-redundant binary manipulators by concatenating Stewart platforms [29], 2RPR-PR parallel modules [30], 3RS parallel manipulators driven by slider-crank linkages [31], or even much simpler one-DOF binary revolute modules [32].

In addition to the previous hyper-redundant robots for manipulation tasks, other robots consisting of many binary actuators have been developed for other tasks. For example, Tadakuma et al. [33] developed a tubular parallel robot consisting of twelve binary dielectric elastomer actuators, which accurately positions a needle for cancer treatment. Lee et al. [34] designed a variable-geometry truss for correcting the shape of solar mirrors. Ding and Yao [35] developed cube-shaped robots whose sides can be modified by three binary actuators. These cubes can be joined to form hyper-redundant lattices able to move through different gaits. A similar mobile robot was presented in [36], which consists of four tetrahedrons joined by a central fifth tetrahedron, where all 18 sides of these tetrahedrons can adopt two possible lengths.

In contrast to the hyper-redundant robots discussed in the previous paragraphs, some researchers have analyzed much simpler binary robots with only a few degrees of freedom. For instance, Schütz, Raatz, and Hesselbach [18, 37] developed and calibrated two binary-actuated parallel robots of types 2RPR and 2PRR, to quickly and accurately reach the four task positions that constitute their discrete workspaces. Zhou [38] analyzed the gait stability of a walking robot with legs made of two serially connected prismatic binary joints. Finally, Chen and Yeo [14] developed the Planar Walker already mentioned in the introduction of this paper, which is a sliding-frame robot consisting of a closed-loop kinematic chain.

With the exception of the Planar Walker [14], which has four binary actuators, previous sliding-frame climbing robots do not employ binary actuators. The reason is that sliding-frame robots typically move thanks to only two or three DOF at most. If these DOF were actuated in a binary manner, the workspace of the robot would consist of only a few sparse poses that prevent the robot from attaining targets with precision [9]. In this paper, we will present a new sliding-frame robot that, despite having only two binary actuators, can reach a very dense workspace to attain target points accurately.

3. Kinematic Analysis

This section describes the kinematics of the proposed mobile robot, which has been named "Xrobin". This name comes from "X-shaped binary robot", where the "X" refers to the crossed configuration adopted by the binary actuators of this robot, as it will become evident later. First, we will analyze the kinematics of the 2RPR-PR closed-chain mechanism, which provides the locomotion of the Xrobin robot. Then, the locomotion of the proposed mobile robot will be described.

3.1. Kinematics of the 2RPR-PR mechanism

Figure 2 represents a 2RPR-PR closed-chain or parallel mechanism. This mechanism is composed of two bodies: A (the base) and B (the platform), which are articulated through a 2-DOF pin-in-slot joint. This joint allows body B to translate

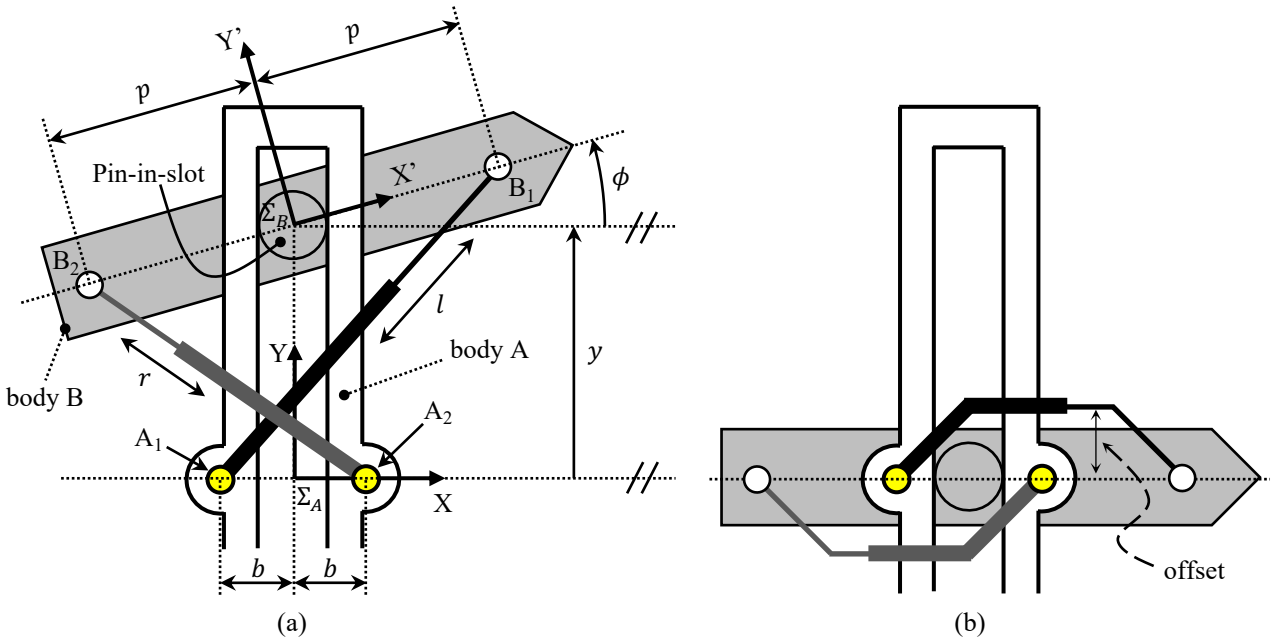

Figure 2: (a) Reference frames and dimensions of the 2RPR-PR closed-chain mechanism. (b) A higher-order singularity of this mechanism, defined by $\phi = y = 0$. Note that the linear actuators are represented with artificial offsets in subfigure (b) in order to avoid overlapping and better observe the singular configuration. In the real robot, these offsets are zero.

(translation y) and rotate (rotation ϕ) with respect to body A. A reference frame Σ_A is attached to body A at its center. Coordinates (y, ϕ) parameterize the position and orientation (pose) of body B relative to body A. The relative pose between bodies A and B can be governed through the extension or retraction of two linear (prismatic) actuators with lengths l and r. Each end of these actuators is connected to bodies A and B through revolute joints A_i and B_i.

The kinematics of the continuously-actuated 2RPR-PR parallel mechanism has been analyzed in previous papers [16, 39, 40], whereas the focus of the present paper will be on the locomotion of the Xrobin regarded as a mobile binary robot. First, however, it is necessary to review the kinematics of the 2RPR-PR mechanism in order to justify the locomotion and advantages of the proposed mobile robot. The starting point is the set of kinematic equations that relate the lengths (l, r) of the linear actuators to the relative pose (ϕ, y) between bodies A and B. According to Figure 2a, the geometric constraints can be derived as follows:

$$(p\cos\phi + b)^2 + (y + p\sin\phi)^2 = l^2 \tag{1}$$

$$(-p\cos\phi - b)^2 + (y - p\sin\phi)^2 = r^2 \tag{2}$$

These two equations simply mean that the distance between the points A_i and B_i should be equal to the lengths of the linear actuators (l, r). The parameters b and p appearing in these equations are the half-widths of bodies A and B, respectively, as illustrated in Figure 2a. These are design parameters to be determined later, so that the robot can achieve the desired configurations.

The forward kinematic problem of this mechanism is defined as computing (ϕ, y) when (l, r) are known. This problem can be solved by manipulating equations (1) and (2) to reduce these to a cubic equation in y^2. This problem has four different real solutions for a generic pair (l, r) [39], as long as the mechanism avoids type-II singularities, which are represented as dashed curves in Figure 3. Figure 3a represents the plane of inputs, where the horizontal axis represents the length of actuator l, whereas the vertical axis represents the length of actuator r. In this figure, the point 11 means that both actuators are completely extended, i.e.: $l = r = \rho_0 + \Delta\rho$, where ρ_0 is the length of the actuators when completely retracted, and $\Delta\rho$ is their stroke. Analogously, point 00 means that the actuators are completely retracted ($l = r = \rho_0$). Similarly, point 01 means that l is retracted and r is extended, whereas point 10 means that l is extended and r is retracted. If the actuators are operated in a binary manner, these four points represent the four possible states for the linear actuators.

For example, for point 11 of Figure 3a, the forward kinematic problem admits the following four solutions [39]:

1. The first solution has the actuators l and r not crossing, with the translation y of body B relative to body A being positive. This solution is represented by point H_{11}^{+} in Figure 3b, and the corresponding posture of the mechanism is represented in Figure 5a. The letter "H" is used for indicating that actuators do not cross in this solution.

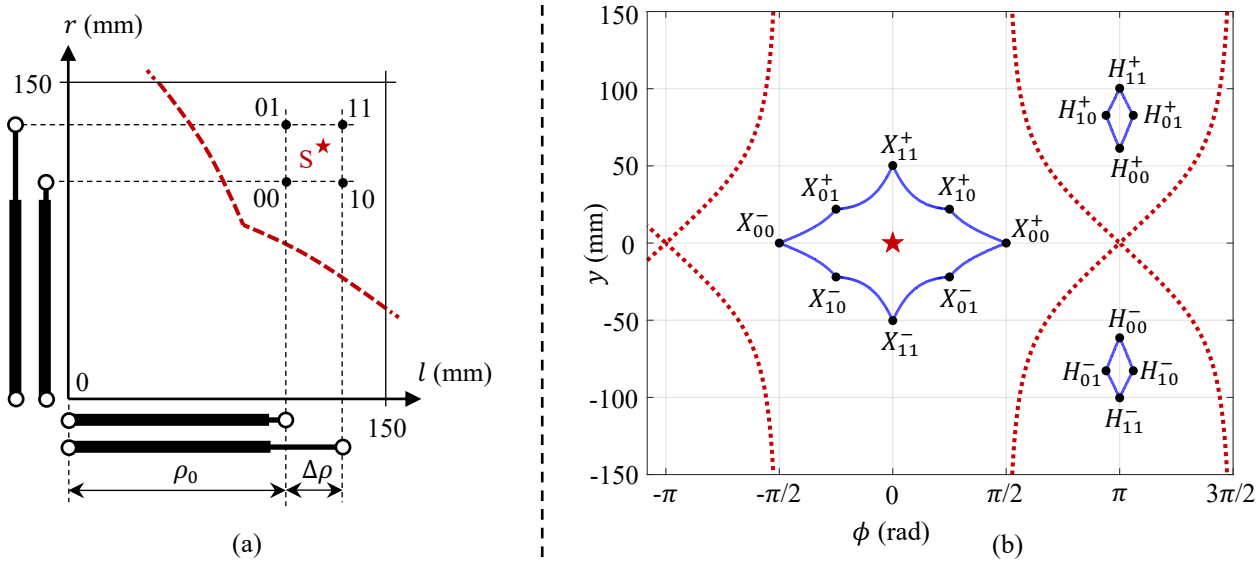

Figure 3: (a) Actuation plane of the 2RPR-PR mechanism. (b) Configuration plane of the 2RPR-PR mechanism.

2. The second solution has actuators l and r crossing, with the translation y being positive. This solution is represented by point X_{11}^{+} in Figure 3b, with the corresponding posture of the mechanism shown in Figure 4a. The letter "X" is used for indicating that the actuators do cross in this solution. Note that this crossing of actuators does not necessarily imply mechanical interferences, since the actuators can lie on parallel planes (see later Section 6).
3. The third solution (point X_{11}^{-} in Figure 3b, posture in Figure 4e) is the mirror image of solution X_{11}^{+} with respect to line A_1-A_2, so it has crossed actuators and negative y.
4. Finally, the fourth solution (point H_{11}^{-} in Figure 3b) is the mirror image of solution H_{11}^{+} with respect to line A_1-A_2, having non-crossed actuators and negative y.

For any other pair (l, r) of Figure 3a different from point 11, other four solutions analogous to these can be identified in a similar manner. Summing up: for each point ij ($i, j \in \{0, 1\}$) of Figure 3a, there exist four solutions, which are represented by the corresponding points H_{ij}^{+}, X_{ij}^{+}, X_{ij}^{-}, and H_{ij}^{-} of Figure 3b. The continuous lines connecting adjacent solutions in Figure 3b are the paths described by the mechanism in the (ϕ, y) plane when only one of the actuators is extended or retracted at a time. For example: retracting actuator r from point 11 to point 10 in Figure 3a, generates the trajectory from X_{11}^{+} to X_{10}^{+} as depicted in continuous line in Figure 3b. All crossed solutions (X_{ij}^{+} and X_{ij}^{-}) are represented in Figure 4, whereas the positive non-crossed solutions (H_{ij}^{+}) are shown in Figure 5. The negative non-crossed solutions (H_{ij}^{-}) are the mirror images of those of Figure 5 with respect to line A_1-A_2.

As demonstrated in [16], the 2RPR-PR mechanism has the ability to travel between the two crossed solutions (X_{ij}^{+} and X_{ij}^{-}) corresponding to a given state ij of the actuators, without traversing type-II singularities at which the mechanism is not fully controllable. In the field of closed-chain and parallel robots, this is called a *nonsingular transition*. In [16], this ability was demonstrated by analyzing closed trajectories in the (l, r) plane of Figure 3a, although the phenomenon can be understood more easily by analyzing trajectories in the (ϕ, y) domain [40, 41]. In any case, the nonsingular transition between any pair of crossed solutions X_{ij}^{+} and X_{ij}^{-} with opposite sign occurs when performing a closed trajectory that starts and ends at some point ij of plane (l, r), as long as this closed trajectory does not cross type-II singularities (i.e., the dashed curves shown in Figure 3a) and encloses once the star-shaped point S shown in Figure 3a, which is a higher-order singularity of this mechanism, at which the dotted lines B_1-B_2 and A_1-A_2 shown in Figure 2a become coincident [16]. The image of point S in the (ϕ, y) plane is the origin, also represented as a star in Figure 3b. The pose of the 2RPR-PR mechanism corresponding to this higher-order singularity is represented in Figure 2b. If the mechanism reaches this singularity, the inverse Jacobian matrix that maps platform velocities $(\dot{\phi}, \dot{y})$ to actuator velocities $(\dot{l}, \dot{r})$ becomes the 2×2 null matrix. This means that the actuators become locked ($\dot{l} = \dot{r} = 0$) while nonzero platform velocities can occur, which implies a loss of stiffness and control at this singularity. This situation is undesirable and is completely avoided by operating the actuators in a binary manner as proposed in Figure 3a, by describing square paths around point S in plane (l, r), extending or retracting only one actuator at a time.

The mentioned nonsingular transitions can be illustrated with the next example. Initially, the mechanism is assumed to have both actuators completely extended (point 11 of Figure 3a), and its initial solution is X_{11}^{+}. By following the closed path 11-10-00-01-11 in Figure 3a, the solution of the mechanism in plane (ϕ, y) will describe the following trajectory: X_{11}^{+}-X_{10}^{+}-X_{00}^{+}-X_{01}^{-}-X_{11}^{-} (Figure 4a-b-c-d-e). In this way, a complete turn about point S in plane (l, r) produces half a turn about the

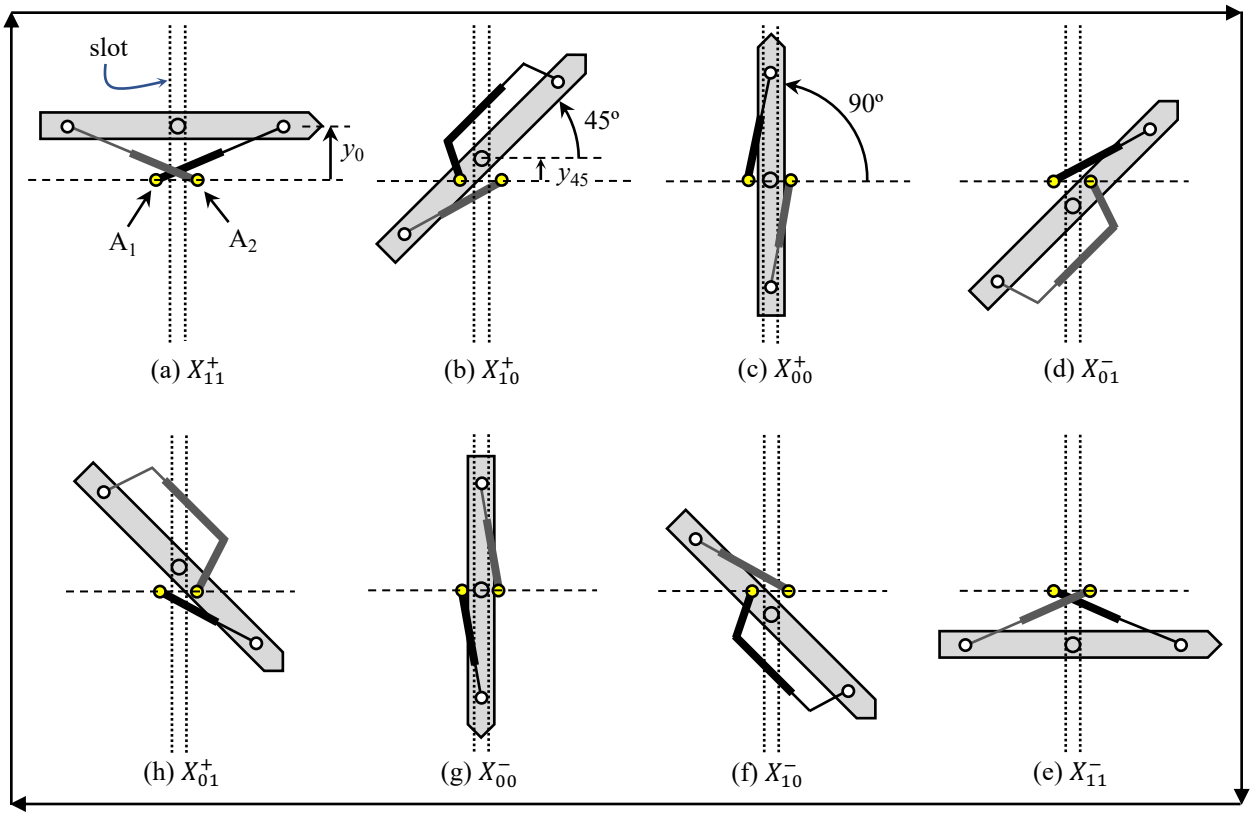

Figure 4: Eight possible configurations $X_{ij}^{\pm}$ of the 2RPR-PR mechanism when assembling it with crossed binary actuators. In this figure, the representation of body A is simplified as a vertical slot for easing the visualization of the postures. Also to ease the visualization and avoid overlappings, some linear actuators in subfigures (b), (d), (f) and (h) include artificial offsets like Figure 2b.

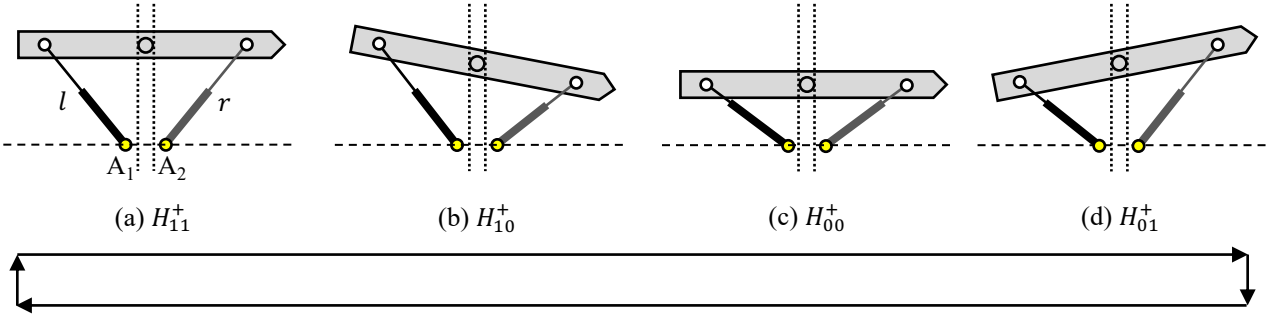

Figure 5: Four possible configurations H_{ij}^{+} of the 2RPR-PR mechanism when assembling it with non-crossed binary actuators (only the positive solutions are shown, the negative solutions H_{ij}^{-} are the mirror images of the positive solutions with respect to line A_1-A_2).

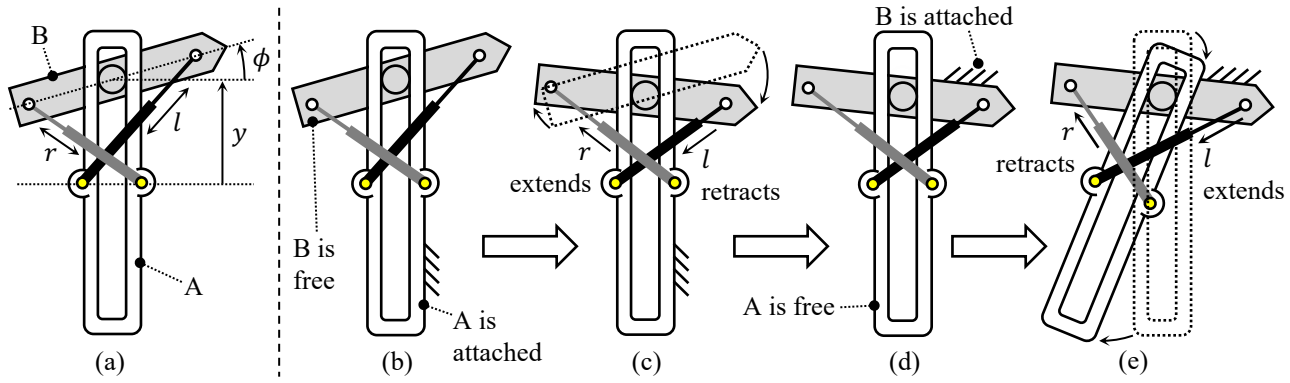

Figure 6: (a) Schematic view of the proposed mobile robot. (b-e) A full locomotion cycle of the proposed mobile robot.

origin in plane (ϕ, y). As noted in [40], repeating again the closed path in plane (l, r) will complete the turn in plane (ϕ, y), returning to the starting solution (X_{11}^{-}-X_{10}^{-}-X_{00}^{-}-X_{01}^{+}-X_{11}^{+}, Figure 4e-f-g-h-a). Note that no type-II singularities (represented by the hourglass-shaped dashed curves in Figure 3b) were traversed during these trajectories, which makes them nonsingular transitions. On the contrary, the non-crossed solutions H_{ij}^{+} and H_{ij}^{-} cannot be connected without traversing these singularities in plane (ϕ, y).

According to the previous example, if the binary-actuated 2RPR-PR mechanism is initially assembled with any crossed solution, then it can visit all eight crossed configurations $X_{ij}^{\pm}$ after completing two turns around point S in plane (l, r). This is twice the number of configurations that one ordinarily expects when operating a robot with $n = 2$ binary actuators. Usually, a robot with n binary actuators can adopt 2^n different configurations. Thus, for a robot with $n = 2$ binary actuators like the 2RPR-PR, one would expect four different configurations. In fact, this is the number of configurations that the mechanism can adopt if assembled with the H^{+} or H^{-} solutions. However, by assembling the mechanism with the crossed solutions X^{+} or X^{-}, the number of configurations reachable with two binary actuators is doubled, since these two crossed solutions can be connected through nonsingular transitions. In this way, the proposed robot can achieve the same number of configurations that would require the use of an additional binary actuator ($n = 3$). Incidentally, many of the hyper-redundant manipulators reviewed in Section 2 of this paper are based on three-DOF parallel modules that can adopt eight different configurations, since they are driven by three binary actuators [21, 26, 28, 31]. Thus, in some sense, the exploitation of nonsingular transitions in the Xrobin robot allows it to effectively spare one binary actuator, with the corresponding savings in costs, weight, consumption, complexity, etc.

3.2. Locomotion of the Xrobin Robot

After explaining the kinematics of the 2RPR-PR mechanism, this subsection outlines the locomotion of the proposed mobile robot. As shown in Figure 6a, the locomotion of the mobile robot is provided by the 2RPR-PR mechanism analyzed in the previous section. The robot has two bodies A and B, connected through a pin-in-slot joint and two linear actuators. This mechanism is assembled with the solution that has these actuators crossed, since it allows the robot to adopt eight different configurations ($X_{ij}^{\pm}$ with $i, j \in \{0, 1\}$) for the four possible combinations of the binary actuators (00, 01, 10, and 11), as explained in the previous section.

Figure 6b-e illustrates a full locomotion cycle of the robot, which is defined as follows. At the beginning of the cycle, body B is free, whereas body A is attached to the plane of motion (Figure 6b). This attachment can be achieved with magnetic adhesion, suction cups, or any other suitable adhesion method. In this situation, each of the linear actuators can be extended or retracted as desired, so that body B will reach a new position and orientation in the plane of motion, as in Figure 6c (if the actuators are binary, then this new pose of body B will be one of the eight possible points $X_{ij}^{\pm}$). After this, body B is attached to the plane of motion, whereas body A is released (Figure 6d). Again, the linear actuators can be extended/retracted, in order to move body A to a new pose, as in Figure 6e (if the actuators are binary, then there are again eight possible poses for body A). Finally, body A is attached again to the plane of motion and B is released, preparing the robot for a new locomotion cycle.

The next section will solve the design problem of this robot, determining the widths of bodies A and B so that it can perform the desired motions when using binary actuators.

4. Kinematic Design

This section determines the dimensions b and p of the robot, in order to achieve the desired postures for motion. As shown in Figure 2a, the parameters b and p are the half-widths of bodies A and B, respectively.

The starting point for the design are the minimum retracted length $\rho_0 > 0$ of the linear actuators, as well as their stroke $\Delta\rho > 0$, since these parameters are usually restricted by the values offered by each manufacturer. In the following, these two parameters are assumed to be known.

Firstly, according to Figure 4a, when both linear actuators are completely extended ($l = r = \rho_0 + \Delta\rho$), the angle ϕ should be zero, and the translation y will be $y_0 > 0$ (to be determined). Substituting these values into equations (1) and (2) yields:

$$(p \cdot 1 + b)^2 + (y_0 + p \cdot 0)^2 = (\rho_0 + \Delta\rho)^2 \tag{3}$$

$$(-p \cdot 1 - b)^2 + (y_0 - p \cdot 0)^2 = (\rho_0 + \Delta\rho)^2 \tag{4}$$

Note that these two equations are the same, so only one of them will be used for the design.

Secondly, according to Figure 4b, when l is completely extended ($l = \rho_0 + \Delta\rho$) and r is completely retracted ($r = \rho_0$), then $\phi = 45°$ and $y = y_{45} > 0$ (to be determined). Substituting these values into Equations (1) and (2) yields:

$$\left(p\frac{1}{\sqrt{2}} + b\right)^2 + \left(y_{45} + p\frac{1}{\sqrt{2}}\right)^2 = (\rho_0 + \Delta\rho)^2 \tag{5}$$

$$\left(-p\frac{1}{\sqrt{2}} - b\right)^2 + \left(y_{45} - p\frac{1}{\sqrt{2}}\right)^2 = \rho_0^2 \tag{6}$$

Finally, according to Figure 4c, when both actuators are completely retracted ($l = r = \rho_0$), then $\phi = 90°$ and $y = 0$. Inserting these values into Equations (1) and (2) yields:

$$(p \cdot 0 + b)^2 + (0 + p \cdot 1)^2 = \rho_0^2 \tag{7}$$

$$(-p \cdot 0 - b)^2 + (0 - p \cdot 1)^2 = \rho_0^2 \tag{8}$$

Again, these two equations are the same. It is not necessary to continue imposing more conditions for the remaining postures of Figure 4: due to symmetry, if Equations (3) to (7) are satisfied, the obtained design will guarantee that all other postures of Figure 4 are reached.

Equations (3), (5), (6) and (7) form a system of 4 independent polynomial equations in 4 unknowns: $\{b, p, y_0, y_{45}\}$, which should all be positive. To solve this system, first we subtract Equation (7) from Equations (3), (5), and (6), obtaining:

$$\begin{array}{llllll} 2 & b \cdot p & & + & y_0^2 & = & k \\ \sqrt{2} & b \cdot p & + \sqrt{2} \quad p \cdot y_{45} & & & = & k - y_{45}^2 \\ \sqrt{2} & b \cdot p & - \sqrt{2} \quad p \cdot y_{45} & & & = & -y_{45}^2 \end{array} \tag{9}$$

where $k = (\Delta\rho + 2\rho_0)\Delta\rho$ is a constant. Equation (9) can be regarded as a linear system in the following three unknowns x_i: $\{x_1 = b \cdot p, x_2 = p \cdot y_{45}, x_3 = y_0^2\}$. The unique solution to this linear system is as follows:

$$p \cdot y_{45} = \frac{\sqrt{2} \cdot k}{4} \longrightarrow p = \frac{\sqrt{2} \cdot k}{4 \cdot y_{45}} \tag{10}$$

$$b \cdot p = \frac{\sqrt{2}}{4}(k - 2\,y_{45}^2) \longrightarrow b = \frac{\sqrt{2}}{4\,p}(k - 2\,y_{45}^2) \xrightarrow{\text{Eq. (10)}} b = \frac{y_{45}}{k}(k - 2\,y_{45}^2) \tag{11}$$

$$y_0^2 = \left(1 - \sqrt{2}/2\right) k + \sqrt{2}\,y_{45}^2 \tag{12}$$

Note that the solution depends on y_{45}^2, which needs to be determined. To determine y_{45}^2, the values of p and b obtained from Equations (10,11) are substituted into Eq. (7), which becomes a polynomial of degree 4 in y_{45}^2:

$$32\left(y_{45}^2\right)^4 - 32\,k\left(y_{45}^2\right)^3 + 8\,k^2\left(y_{45}^2\right)^2 - 8\,k^2\rho_0^2\left(y_{45}^2\right) + k^4 = 0 \tag{13}$$

The roots of Equation (13) will depend on k, which in turn depends on ρ_0 and $\Delta\rho$. For example, for $\rho_0 = 103$mm and $\Delta\rho = 27$mm (these are the values that will be used in the prototype described later in Section 6), the quartic polynomial Equation (13) has two non-real roots and two real positive roots, which are:

$$y_{45}^2 = 482.01\text{mm}^2 \text{ (first solution)} \quad OR \quad y_{45}^2 = 6909.37\text{mm}^2 \text{ (second solution)} \tag{14}$$

The second solution is not valid because it yields $b < 0$ when back-substituted into (11), but b should be positive. Thus, only the first solution is valid, which yields the following design when back-substituted into (10) and (11): $p = 101.31$mm, $b = 18.59$mm. These are the values used for designing the prototype that will be described in Section 6. Finally, as a final check, one can also compute y_0 from (12), obtaining: $y_0 = 50.24$mm. This value of y_0 is useful for dimensioning the length of the central slot of body A of the robot, to guarantee that this slot will be long enough to allow body B to slide along it without reaching the mechanical limits of the slot.

5. Workspace Analysis

This section analyzes the workspace of the Xrobin mobile robot. If the robot uses binary actuation, the workspace will be a point cloud consisting of a finite number of discrete poses. In fact, the workspace of the binary 2RPR-PR mechanism has already been represented in Figure 3b, which represents a workspace consisting of 16 points ($X_{ij}^{\pm}$ and $H_{ij}^{\pm}$). As explained previously, points $X_{ij}^{\pm}$ are attainable only when the mechanism is assembled with the crossed solution, points H_{ij}^{+} are reachable when assembling the mechanism with non-crossed solution (with positive displacement y), and H_{ij}^{-} are reachable when assembling it with the non-crossed solution (with negative displacement y). In the following, it will be assumed that the robot is assembled with the crossed solution, so that the workspace of the 2RPR-PR mechanism will consist of the eight points $X_{ij}^{\pm}$ shown in Figure 3b.

Although the binary 2RPR-PR mechanism with crossed actuators can only attain eight different configurations, it must be noted that the workspace of the mobile robot will consist of a much larger and denser set of positions. Indeed, consider a single motion cycle of the binary robot, as illustrated in Figure 6. At the beginning of the cycle, body A is fixed to the ground, and the actuators are extended or retracted to achieve one of the eight possible configurations $X_{ij}^{\pm}$ of the mechanism, from those shown in Figure 3b. This will place body B in a new pose. After this, body B is fixed to the ground and body A is released. Then, the actuators are again retracted or extended to achieve a second configuration of the mechanism, among those points $X_{ij}^{\pm}$ of Figure 3b. Since body B is fixed, this second configuration of the mechanism will place body A in a new pose. Finally, body A is fixed again to the ground and body B is released, and the robot is ready to begin a new motion cycle.

After a single motion cycle, body A can reach up to $8^2 = 64$ possible poses, due to the eight possible motions of B relative to A during the first half of the cycle, multiplied by the eight possible motions of A relative to B during the second half of the cycle. If we repeat this cycle taking any of these 64 poses of body A as the new starting pose, this will generate 64 new poses after the new cycle, and so on. As a result, by recursively executing more and more cycles, more attainable poses are added to the point cloud and the workspace becomes larger and denser, allowing the mobile binary robot to reach an almost continuous workspace. This will be shown in the remainder of this section. More precisely, after executing up to N cycles, the number of possible poses for body A will be:

$$\text{Number of poses for body A} = \sum_{i=1}^{N} 64^i \tag{15}$$

For example: after $N = 2$ cycles, body A can reach 64 poses after the first cycle, plus 64^2 more poses after the second cycle (i.e., 64 poses reachable from each of the 64 poses generated after the first cycle).

First, a reference frame Σ_A is attached to the center of body A, as shown in Figure 2a. The pose (position and orientation) of this reference frame can be parameterized by its position (x_A, y_A) and orientation ϕ_A with respect to some inertial reference frame Σ_W attached to the ground. The transformation from local coordinates in frame Σ_A to global coordinates in frame Σ_W is given by the following planar homogeneous transformation matrix:

$${}^{W}\mathbf{T}_{A}(x_A, y_A, \phi_A) = \begin{bmatrix} \cos\phi_A & -\sin\phi_A & x_A \\ \sin\phi_A & \cos\phi_A & y_A \\ 0 & 0 & 1 \end{bmatrix} \tag{16}$$

Consider also a frame Σ_B attached to body B, centered at the pin-in-slot joint and with axis X' directed along B_1B_2, as shown in Figure 2a. The matrix ${}^{W}\mathbf{T}_{B}$ that encodes the pose of frame Σ_B relative to frame Σ_W can be obtained as follows:

$${}^{W}\mathbf{T}_{B} = {}^{W}\mathbf{T}_{A} \cdot {}^{A}\mathbf{T}_{B} \quad \text{, where:} \quad {}^{A}\mathbf{T}_{B}(\phi, y) = \begin{bmatrix} \cos\phi & -\sin\phi & 0 \\ \sin\phi & \cos\phi & y \\ 0 & 0 & 1 \end{bmatrix} \tag{17}$$

${}^{A}\mathbf{T}_{B}(\phi, y)$ is the transformation matrix that encodes the position and orientation of body B relative to body A. It depends on the internal degrees of freedom (ϕ, y) of the 2RPR-PR mechanism, which in turn depend on the actuated lengths (l, r) through Equations (1) and (2).

In what follows, the N-workspace (or N-cycle workspace) of the Xrobin robot will be defined as the set of positions (x_A, y_A) that the center of body A can reach after N motion cycles, considering a binary operation of the actuators. The N-workspace can be calculated with Algorithm 1. This algorithm presents two routines: a main routine `WORKSPACE` (lines 1-3) and a recursive subroutine `CYCLE` (lines 4-17).

The inputs to routine `WORKSPACE` are the number N of cycles, and the m discrete configurations of the 2RPR-PR mechanism, stored as vectors $\mathbf{Y} = [y_1, \ldots, y_m]$ and $\mathbf{\Phi} = [\phi_1, \ldots, \phi_m]$ that contain the coordinates of these m discrete configurations considered as points of the (ϕ, y) plane, as shown in Figure 3b. For example, if the robot is assembled with the crossed solution, there will be m=8 configurations, and (ϕ_k, y_k) $(k = 1 \ldots m)$ will be the coordinates of points $X_{ij}^{\pm}$ in the plane (ϕ, y) shown in

Figure 3b. Similarly, if the robot is assembled with the non-crossed solution with positive displacement y, there will be $m = 4$ configurations, and in that case (ϕ_k, y_k) will be the coordinates of points H_{ij}^{+} in the plane (ϕ, y) shown in Figure 3b.

The output of `WORKSPACE` is a point cloud $\mathcal{WS}$ that will store all the poses (positions AND orientations) reachable by the binary robot after N motion cycles. Note that $\mathcal{WS}$ will be updated inside the recursive routine `CYCLE`, which will add more and more points to $\mathcal{WS}$ as they are computed. Therefore, $\mathcal{WS}$ should be interpreted in Algorithm 1 as a passed-by-reference variable (instead of a passed-by-value one).

The inputs to subroutine `CYCLE` are the position (x_A, y_A) and orientation ϕ_A of body A at the beginning of the cycle, the vectors $\mathbf{Y}$ and $\mathbf{\Phi}$ which store the m discrete configurations of the 2RPR-PR mechanism (exactly as in routine `WORKSPACE`), the index n that identifies the current cycle, the number N of cycles to execute, and the global point cloud $\mathcal{WS}$ that stores all workspace points computed during the whole execution of Algorithm 1. As explained above, $\mathcal{WS}$ is passed by reference to routine `CYCLE`. This routine has no outputs, since its main result is stored in the global variable $\mathcal{WS}$.

Algorithm 1 Method to compute the workspace of the Xrobin robot after N cycles.

1: **procedure** WORKSPACE(N,$\mathbf{Y}$,$\mathbf{\Phi}$)
   Inputs:
   - N : number of cycles
   - $\mathbf{Y} = [y_1, \ldots, y_m]$, $\mathbf{\Phi} = [\phi_1, \ldots, \phi_m]$: configurations of 2RPR-PR mechanism

   Outputs:
   - $\mathcal{WS}$: point cloud of discrete workspace

2: $\mathcal{WS} \leftarrow \emptyset$ // initialized as the empty set
3: `CYCLE`$(0, 0, 0, \mathbf{Y}, \mathbf{\Phi}, 1, N, \mathcal{WS})$

4: **procedure** CYCLE(x_A,y_A,ϕ_A,$\mathbf{Y}$,$\mathbf{\Phi}$,n,N,$\mathcal{WS}$)
   Inputs:
   - (x_A, y_A, ϕ_A) : pose of body A at the beginning of the cycle
   - $\mathbf{Y} = [y_1, \ldots, y_m]$, $\mathbf{\Phi} = [\phi_1, \ldots, \phi_m]$: configurations of 2RPR-PR mechanism
   - n : index of current cycle $(1 \leq n \leq N)$
   - N : number of cycles
   - $\mathcal{WS}$: point cloud of discrete workspace (variable passed by reference)

   Outputs:
   - No outputs.

5: **if** $n \leq N$ **then**
6: $m \leftarrow$ `length`$(\mathbf{Y})$
7: **for** $i = 1 \ldots m$ **do**
8: $(y_i, \phi_i) \leftarrow i$-th element of vectors $\mathbf{Y}$ and $\mathbf{\Phi}$
9: ${}^{W}\mathbf{T}_{B} \leftarrow {}^{W}\mathbf{T}_{A}(x_A, y_A, \phi_A) \cdot {}^{A}\mathbf{T}_{B}(\phi_i, y_i)$
10: **for** $j = 1 \ldots m$ **do**
11: $(y_j, \phi_j) \leftarrow j$-th element of vectors $\mathbf{Y}$ and $\mathbf{\Phi}$
12: $\mathbf{P} \leftarrow {}^{W}\mathbf{T}_{B} \cdot \left({}^{A}\mathbf{T}_{B}(\phi_j, y_j)\right)^{-1}$
13: $x_0 \leftarrow$ element (1,3) of $\mathbf{P}$
14: $y_0 \leftarrow$ element (2,3) of $\mathbf{P}$
15: $\phi_0 \leftarrow$ arctan2($\mathbf{P}(2,1), \mathbf{P}(1,1)$) // arctangent of two arguments
16: Add $[x_0, y_0, \phi_0]$ to $\mathcal{WS}$
17: `CYCLE`$(x_0, y_0, \phi_0, \mathbf{Y}, \mathbf{\Phi}, n+1, N, \mathcal{WS})$

Taking this into account, the overall behavior of Algorithm 1 is as follows. First, $\mathcal{WS}$ is initialized as the empty set (line 2). Then, line 3 calls `CYCLE` for the first time, passing the initial pose of body A (which is assumed to be at the origin, with a zero orientation) and the index indicating that the first motion cycle should be performed ($n = 1$).

Once inside `CYCLE`, new poses will be generated for body A if n does not exceed N (line 5). New poses for A are generated as follows. Adopting each of the m possible configurations of the 2RPR-PR mechanism (lines 7-8), body B is moved to a new pose assuming that body A is fixed (line 9). This completes the first half of the motion cycle. Then, after this motion, body B is fixed, body A is released, and body A is moved to a new pose, corresponding to each of the m possible postures of body B relative to body A of the 2RPR-PR mechanism (lines 10-12). This completes the second half of the motion cycle. The new pose adopted by body A after the motion cycle is encoded in matrix $\mathbf{P}$. The position and orientation coordinates $[x_0, y_0, \phi_0]$ are extracted from this matrix and added to the workspace point cloud $\mathcal{WS}$ (lines 13-16). Finally, a new cycle is executed recursively on line 17, starting from the newly computed pose of body A, and increasing the index of the cycle $(n + 1)$.

Table 1: Geometric parameters of the designed robot.

Symbol	Definition	Value (mm)
b	Half width of body A	18.59
p	Half width of body B	101.31
ρ_0	Actuator retracted length	103
$\Delta\rho$	Actuator stroke	27

Next, this algorithm will be illustrated for the design that was obtained in section 4, which is summarized in Table 1. For this design, assuming that the linear actuators are binary, the 2R$\underline{\text{P}}$R-PR mechanism assembled with crossed solution can adopt the following eight configurations (ϕ_k, y_k):

$$\mathbf{\Phi} = [\phi_1, ..., \phi_8] = [0, -\pi/4, -\pi/2, -\pi/4, 0, \pi/4, \pi/2, \pi/4]\,\text{rad} \tag{18}$$

$$\mathbf{Y} = [y_1, ..., y_8] = [50.242, 21.955, 0, -21.955, -50.242, -21.955, 0, 21.955]\,\text{mm} \tag{19}$$

When plotted in plane (ϕ, y), these eight configurations are the points $X_{ij}^{\pm}$ represented in Figure 3b. Introducing these eight configurations to routine `WORKSPACE` generates the workspaces shown in Figure 7, for $N = 1, 2, 3, 4$ cycles. Figure 7a includes a scaled representation of the robot, to compare its size with that of the workspaces. As predicted by (15), the number of workspace points for $N = 4$ cycles is 17,043,520, denoting a high maneuverability.

All the workspaces represented in Figure 7 consist of discrete positions that can be reached by the center of body A of the robot when its actuators are binary. Despite using binary actuators, however, note in Figure 7c-d that the density of points near the origin (which is the starting position of the robot before executing the first cycle) is so high that it makes the workspace *look almost* continuous for $N \geq 3$ cycles. Obviously, this is only a visual effect caused by the resolution of the figure, since zooming-in the area near the origin shows that these workspaces still are discrete (this is shown in the 20×20mm insets (e) and (f) in Figure 7c-d). Even if these workspaces are discrete, their high density of points promises a high positional resolution. One should expect to obtain an even higher resolution near the origin when increasing further the number N of motion cycles, up to a limit to be determined (one should not expect the workspace to completely fill the xy plane even if $N \to \infty$, there will always be small unreachable voids). In any case, even if we could reach an extremely fine theoretical resolution after a large number of cycles N, the actual positional resolution in practice will be limited by the hardware of the real implementation of the robot (resolution of sensors, noise, slip or friction effects, flexibility of links, joint clearances, etc.).

Note that Algorithm 1 does not only store the positions (x_A, y_A) reachable by the center of body A, but also the orientation ϕ_A with which each position is reached. When plotting the workspaces in Figure 7, we omitted the orientation with which each point was reached, which results in the *reachable* or *maximal* workspace, which is the set of positions that can be reached with some orientation, without caring which one. If one cares about the orientation with which each position is reached, the best option to analyze the workspace of this robot is to plot the *constant-orientation* workspace, which is defined as the set of positions that can be reached with a precise orientation. The Xrobin robot, due to its binary actuation and its design, can reach orientations that are multiples of 45°. Thus, for this robot, eight constant-orientation workspaces can be represented, corresponding to the eight multiples of 45° that can be found in the interval $[-180°, 180°)$: $\{-180°, -135°, -90°, -45°, 0°, 45°, 90°, 135°\}$. These eight constant-orientation workspaces are represented in Figure 8, for $N = 3$ cycles. These eight workspaces can be obtained by dividing the reachable workspace of Figure 7c into different sets depending on the orientation with which each position was reached. Note that the overlapping union of these eight constant-orientation workspaces results in the point cloud shown in Figure 7c, which is the maximal workspace that contains all positions that can be reached regardless of the orientation.

All constant-orientation workspaces in Figure 8 are similar. Figure 8e shows the workspace for a zero orientation, with its convex hull in dashed line. This zero-orientation convex hull is reproduced in the remaining subfigures of Figure 8, to make clearer the comparison of the relative size and shape of the zero-orientation workspace with the other constant-orientation workspaces. In all cases, the density of points near the origin is high, which means that the robot can practically reach any point near the origin (up to the positional resolution imposed by the discrete nature of these workspaces) with any orientation multiple of 45°. Note that the fact that this density is high only near the origin is not a limitation, since any position P can be "reset" to become the new origin or starting position of the robot after reaching P (the workspace "moves" with the robot), allowing the robot to reach the points near P with the same accuracy that it can reach the points near the origin in Figure 7c-d.

Summing up: in spite of the binary actuation, according to Figures 7 and 8, the proposed Xrobin robot has a high maneuverability, in the sense that it can reach a wide and dense range of discrete positions with orientations multiple of 45° after a few motion cycles, up to the resolution imposed by the binary actuation. This high maneuverability is especially evident when compared with the workspace of the robot if it was assembled with a non-crossed solution, such as the H_{ij}^{+} solutions, as it will be demonstrated next.

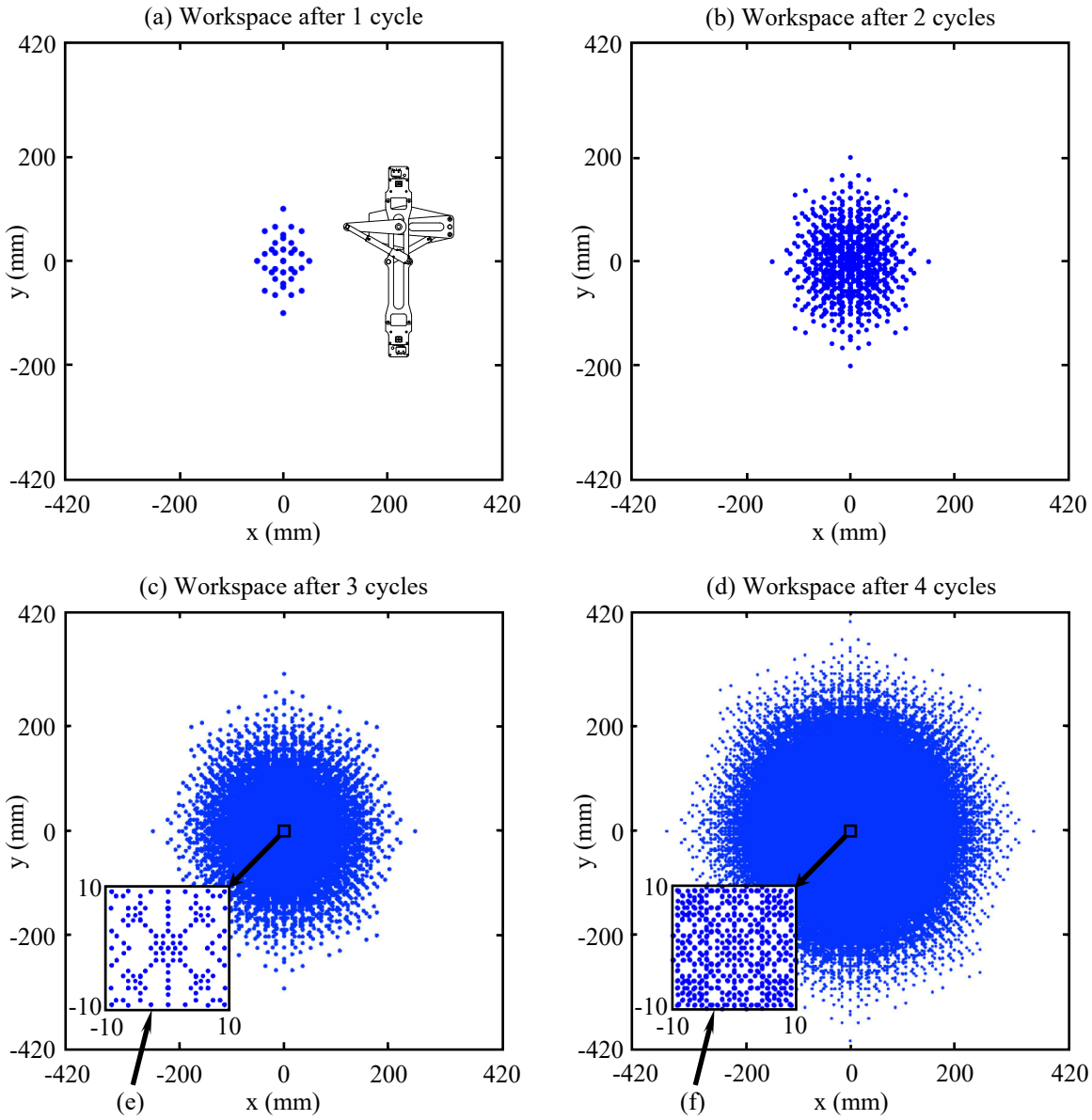

Figure 7: Reachable workspaces for body A after (a) one cycle, (b) two cycles, (c) three cycles, and (d) four cycles.

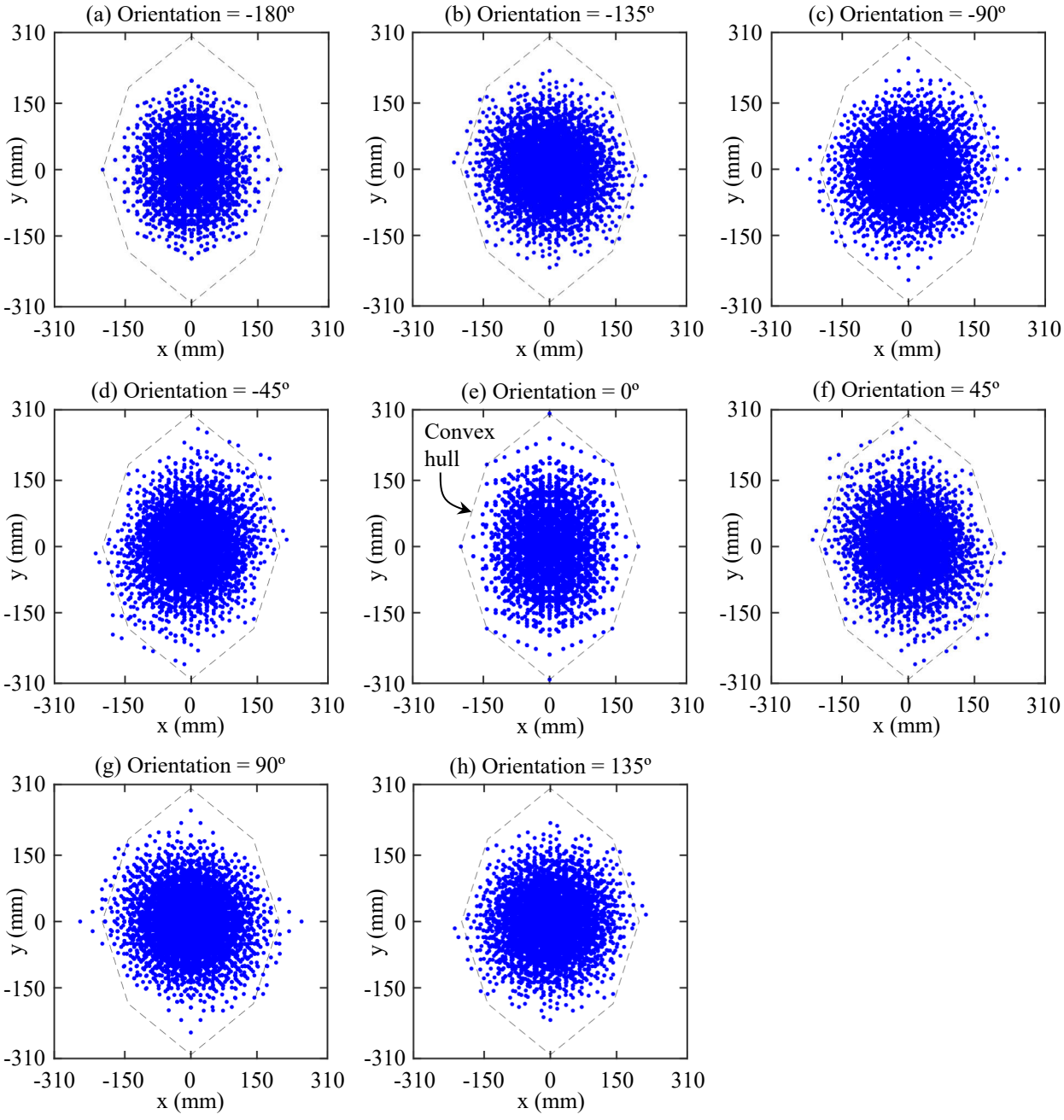

Figure 8: Constant-orientation workspaces for $N = 3$ cycles.

5.1. Comparison With Non-crossed Robot

If the robot is assembled with the non-crossed solution H^+, then there are only four possible configurations or relative poses between bodies A and B, which are given by the points H^+_{ij} of Figure 3b. The coordinates (ϕ_k, y_k) of these points are:

$$\mathbf{\Phi} = [\phi_1, ..., \phi_4] = [\pi, 2.952, \pi, 3.330]\,\text{rad} \tag{20}$$

$$\mathbf{Y} = [y_1, ..., y_4] = [100.29, 82.74, 61.38, 82.74]\,\text{mm} \tag{21}$$

By inputting these four configurations to Algorithm 1, the reachable workspaces represented in black in Figure 9 are obtained. These workspaces are overlapped with those of the crossed robot, which are represented in gray in the same figure (these gray workspaces are the same shown in Figure 7). By comparing the workspaces of both types of robot, it is clear that the workspaces of the non-crossed robot are more asymmetric and much smaller than those of the crossed robot. Moreover, the density of points of the non-crossed workspaces is much less uniform, leaving larger voids than the crossed robot. All of this clearly illustrates the advantages of choosing the crossed solution to assemble the Xrobin robot, in order to exploit nonsingular transitions and reach a larger, denser, and more symmetric workspace.

5.2. Comparison With Traditional Serially-Actuated Sliding-Frame Robot

The proposed robot with crossed actuators can also be compared with an "equivalent" serially-actuated sliding-frame robot with polar topology, like those analyzed in the introduction of this paper and schematized in Figure 1b. These robots consist of two bodies connected through a pin-in-slot joint like the proposed robot, but in these robots this joint is serially actuated, whereas in the proposed robot this joint is passive and driven by a 2RPR-PR parallel linkage. Such an equivalent serial robot can be obtained from the proposed robot by removing the crossed actuators as shown in Figure 10a, and directly actuating the translational and rotational degrees of freedom of the pin-in-slot joint by a piston and a rotary motor, respectively.

Assuming that this piston and rotary motor are binary, the equivalent serial robot can only adopt four possible configurations, which are represented in Figure 10a. In this case, to make a fair comparison with the Xrobin robot, the binary piston of the equivalent serial robot should only adopt two positions: $y = 0$ or $y = 100.48$ mm, which is the maximum distance that the Xrobin robot can advance in a single motion cycle. Also, the binary rotary motor of the serial robot should be able to adopt only two angular positions: $\phi = 0$ and $\phi = 45°$, since the Xrobin robot can only adopt orientations multiple of 45°.

Figure 10b compares the workspace of the Xrobin robot (in gray) with that of the equivalent serial binary robot (in black), after four motion cycles. As this figure shows, the shape and size of both workspaces are similar, but the workspace of the proposed robot is much denser than that of the traditional serially-actuated equivalent robot, demonstrating higher precision. The 4-cycle workspace shown in Figure 10b for the proposed robot consists of 17,043,520 points, whereas that of the traditional robot only has 69,904 points (this number is obtained after changing 64 for 16 in Equation (15)). One may question if increasing the number of motion cycles for the traditional robot would allow it to reach targets with an accuracy comparable to that of the proposed robot. For example, let us increase the number of motion cycles for the traditional robot up to $N = 7$ cycles, which generates 286,331,152 reachable points (for more cycles, our computer runs out of memory due to having to store too many workspace points). In that case, the 7-cycle workspace of the traditional robot is represented in Figure 10c in black, overlapped on the 4-cycle workspace of the proposed robot. Only the points in the box $[-200, 200]\times[-200, 200]$ are represented in Figure 10c, since this is the approximate area in which the workspace of the proposed robot looks almost continuous. This box contains 202,174,145 workspace points for the traditional robot (70.61% of the total), while it contains 16,983,602 points for the proposed robot (99.65% of the total). Note that, despite this large difference between the number of points contained in the same box for the traditional and for the proposed robot (202 versus 17 million), the workspace of the proposed robot is still much denser than the traditional one, because most of the workspace points of the traditional robot are repeated. This makes our robot more efficient since it can reach targets with higher precision requiring even fewer movements (4 cycles instead of 7). Both robots have the same number of binary actuators, but our proposed robot makes a better use of these actuators in order to reach a denser workspace. The comparisons shown in this section further illustrate the advantages of using a 2RPR-PR closed-chain linkage that exploits nonsingular transitions to drive the proposed robot, instead of using a more traditional serial actuation scheme like previous sliding-frame robots.

Summing up, the advantages of our proposed robot are as follows. By exploiting nonsingular transitions, and using only two binary actuators arranged in a crossed manner, our proposed robot can adopt the same number of configurations ($2^3 = 8$) as traditional robots that would require three binary actuators, which effectively saves an actuator, with the corresponding savings in weight, consumption, and complexity. Moreover, the N-cycle workspace of our robot exhibits a high symmetry and density, allowing it to reach nearby targets accurately with any orientation multiple of 45°. Furthermore, as illustrated in Figure 10c, the proposed robot requires fewer movements in order to reach targets more accurately than traditional serially-actuated binary robots having equivalent ranges of motion, which also reduces energy consumption. These advantages make our robot especially suitable for tasks that require moving a robot along a plane of motion. Some typical application scenarios that involve such motions, in which the proposed robot can be useful, are listed next. As stated in the introduction of this paper,

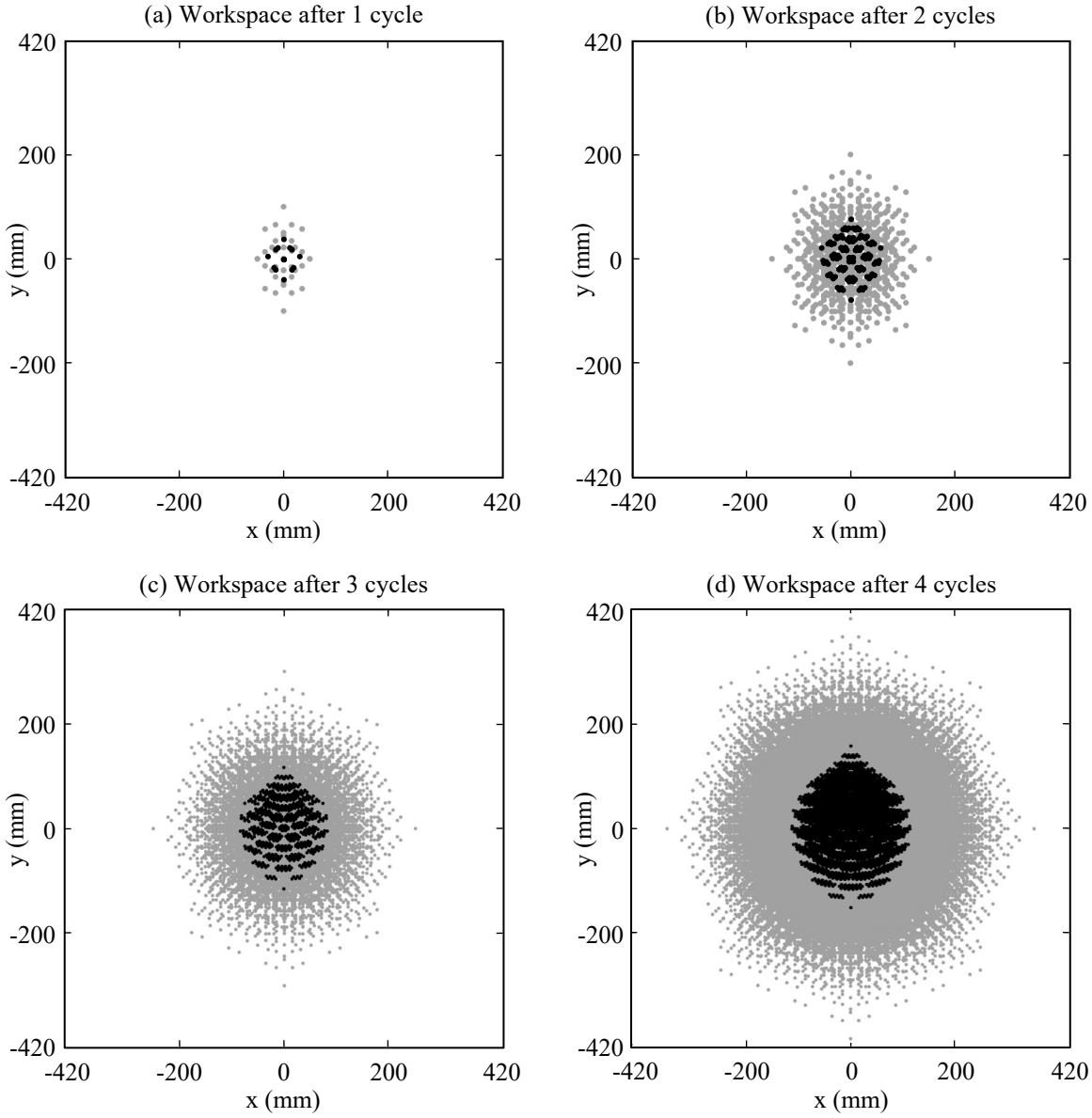

Figure 9: Comparison of the reachable workspace for a non-crossed robot (in black) and a crossed robot (in gray).

typically, these are tasks that must be performed at considerable heights, which make them dangerous for human operators that may get hurt by falling from height:

- Cleaning of vertical glass facades. By using suction cups to attach/detach bodies A and B, and adding brushes to body B, the proposed robot can be used for cleaning glass facades. The dense area coverage of the proposed robot despite using binary actuation would allow it to exhaustively clean the plane over which it moves.

- Nondestructive testing of metallic structures such as construction beams, ship hulls, vessels, etc. By using magnetic adhesion, the proposed robot can climb planar (or approximately planar) metallic surfaces in order to inspect them visually with a camera, for identifying superficial cracks or assessing the state of coating layers that protect against corrosion. By equipping body B with an ultrasonic probe, it can also be used for scanning (e.g., by moving body B while A is attached) and detecting internal cracks, or measure the thickness of the metallic surface to assess its degree of corrosion. The possibility of accurately placing the proposed robot at almost any target position with the simplicity of only two binary actuators would avoid missing cracks that a more traditional binary robot may miss, due to its coarser walking step.

6. Experimental Prototype

This section will describe the development of a real prototype of the Xrobin robot, as well as the testing of this prototype, to demonstrate that the robot proposed in this paper can be realized physically, avoiding collisions between different mechanical parts while traveling through all the discrete configurations $X_{ij}^{\pm}$ shown in Figure 3b.

A CAD model of the prototype is shown in Figure 11. It can be checked that the top view of the robot looks like the 2RPR-PR mechanism schematized earlier in Figure 2a. The robot consists of the two bodies A and B, interconnected through a central pin-in-slot joint and two linear actuators.

Figure 12 shows the isolated views of bodies A and B. As Figure 12a shows, the geometry of body A is quite simple, since it consists basically of the slot along which body B slides. At both ends, body A has magnetic devices to adhere to ferromagnetic surfaces (these devices will be explained later).

While body A is quite simple, the design of body B is a bit more complex. In fact, the mechanical design of body B was one of the most challenging parts of the development of this prototype, since it should satisfy the following requirements while avoiding mechanical interferences between different moving parts:

- The bottom part of body B should be in contact with the ground in order to make it possible for the robot to adhere to it.

- Body A and body B should be articulated through a pin-in-slot joint.

- The linear actuator l should be connected between bodies A and B.

In order to satisfy these conditions, the final design of body B was inspired by crankshafts, as it can be seen in Figure 12b.

Regarding the linear actuators, these are from manufacturer Actuonix. The model of the actuators is: L12-50-210-12-P. These actuators are powered by a 12 Vdc motor, they have a reduction gear with ratio 210:1, their minimum retracted length is 102mm, and their available stroke is 50mm. They possess a potentiometer to measure the degree of extension of the actuator. In our robot, these actuators were operated in a binary manner, using the following values for the retracted length and for the stroke: $\rho_0 = 103$mm and $\Delta\rho = 27$mm. Accordingly, these values are within the limits set by the manufacturer.

6.1. Adhesion Technology

As explained in Figure 6b-e, the Xrobin robot moves by adhering one of the bodies to the ground and moving the other body to a new pose, then swapping the roles of the attached/free bodies, and repeating this process until reaching the desired pose. Thus, it is necessary to provide these bodies with means to adhere to (or detach from) the plane of motion at will.

Of all adhesion technologies used in robotics, the most mature ones are mechanical gripping, pneumatic suction, and magnetic adhesion [1]. Mechanical gripping usually requires the robot to access both sides of the gripped object. However, this is not possible in the field of application of the Xrobin robot, which will move on planar surfaces with only one accessible side, which poses a situation for which pneumatic and magnetic adhesion are more suitable. Since the main application of the Xrobin robot will be to climb and inspect steel surfaces, magnetic adhesion was considered as the best option.

The traditional way of providing robots with switchable magnetic adhesion forces (i.e., forces that can be switched ON/OFF as required by bodies A and B of our robot) has been through electromagnets, which produce adhesion only while they are electrically powered. Recently, however, there has been an increase in the use *switchable permanent magnets* in robotics [42]. Such devices consist of permanent magnets which can be mechanically rotated to redirect the magnetic flux through an external surface (producing the adhesion to it), or through an internal magnetic circuit (disabling the adhesion to

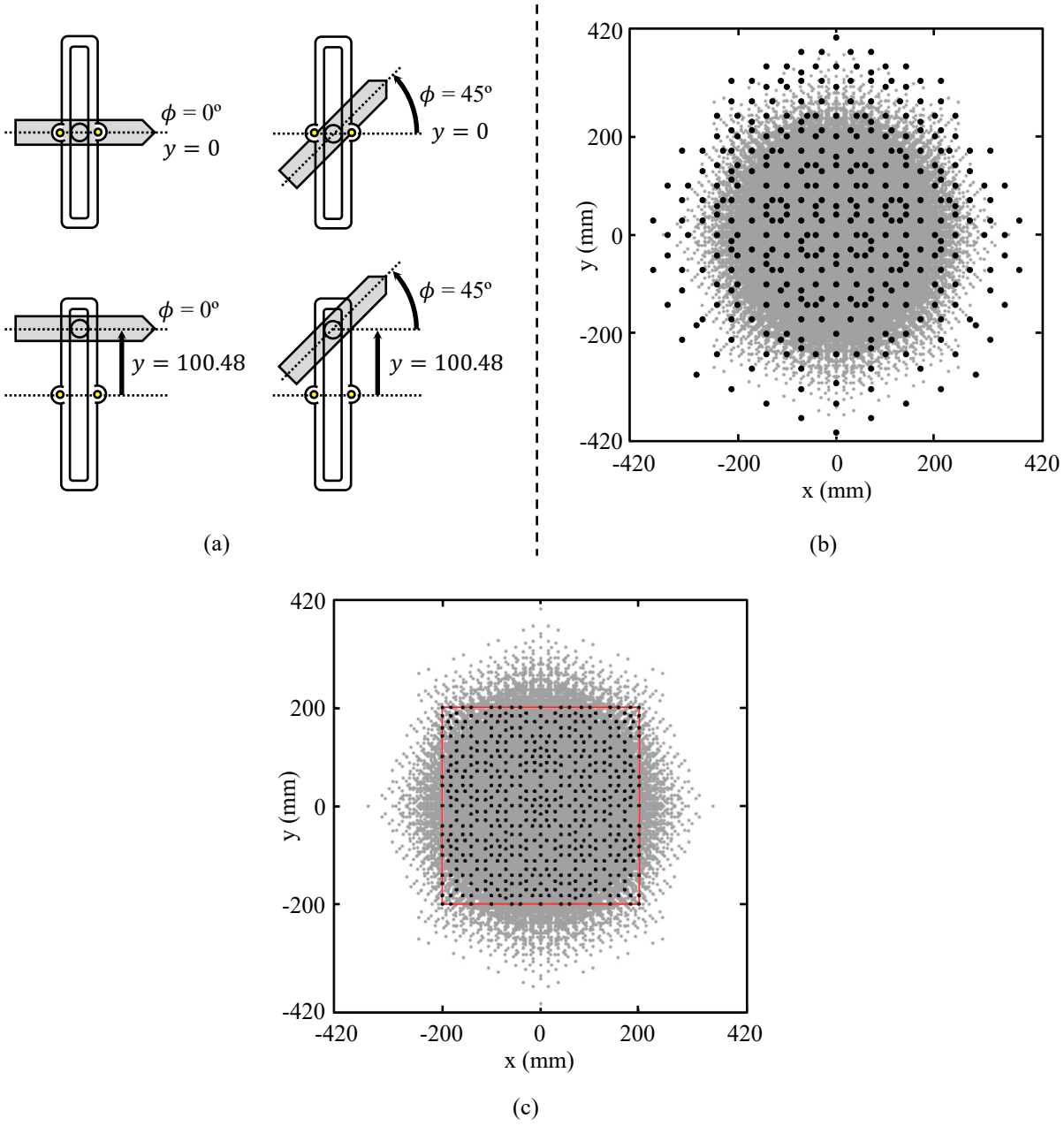

Figure 10: (a) Four possible configurations for a traditional serial binary-actuated sliding-frame robot equivalent to the proposed parallel robot. (b) Comparison of the reachable workspace after 4 cycles, for the proposed robot (in gray) and the equivalent serial binary robot (in black). (c). Comparison of the 4-cycle workspace of the proposed robot (in gray) and the 7-cycle workspace of the traditional robot (in black, only points in $[-200, 200] \times [-200, 200]$).

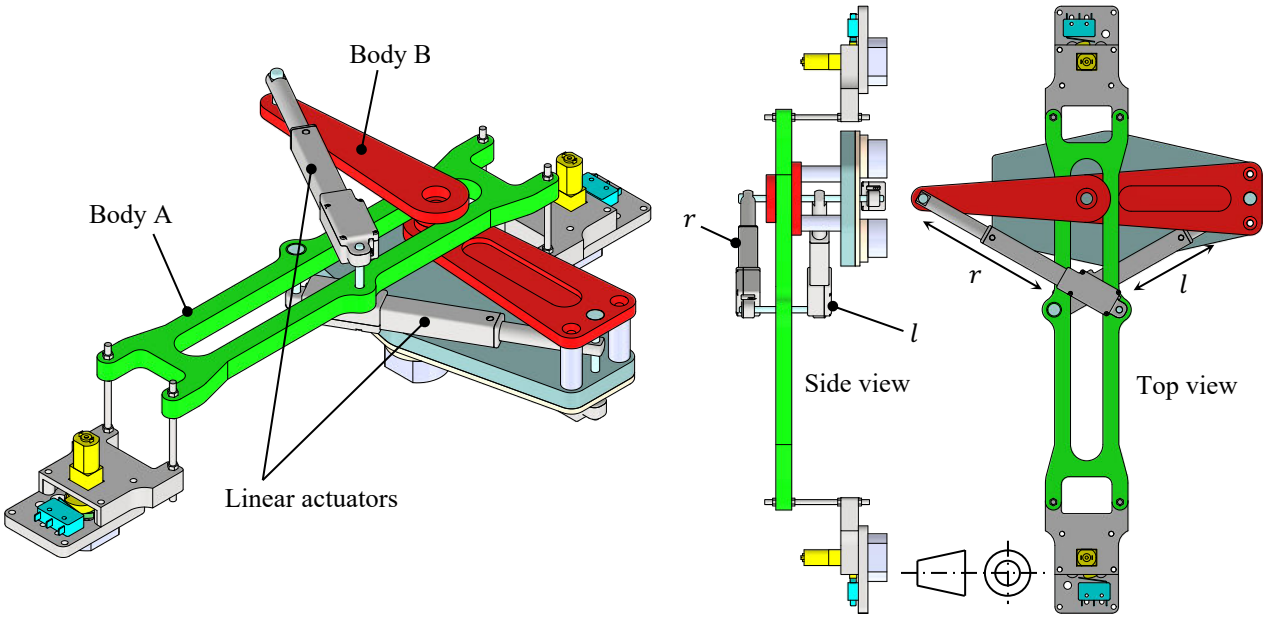

Figure 11: CAD representation of the Xrobin robot.

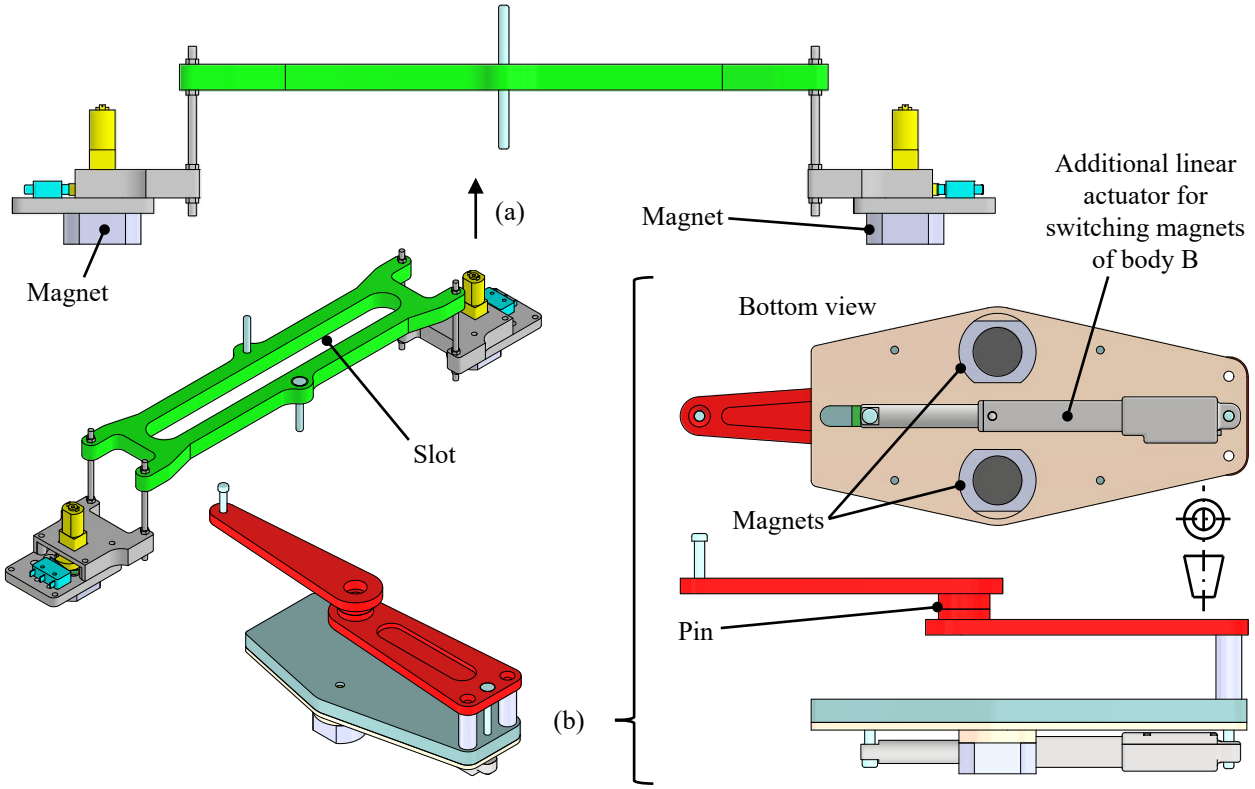

Figure 12: Isolated views of the CAD designs of bodies (a) A and (b) B.

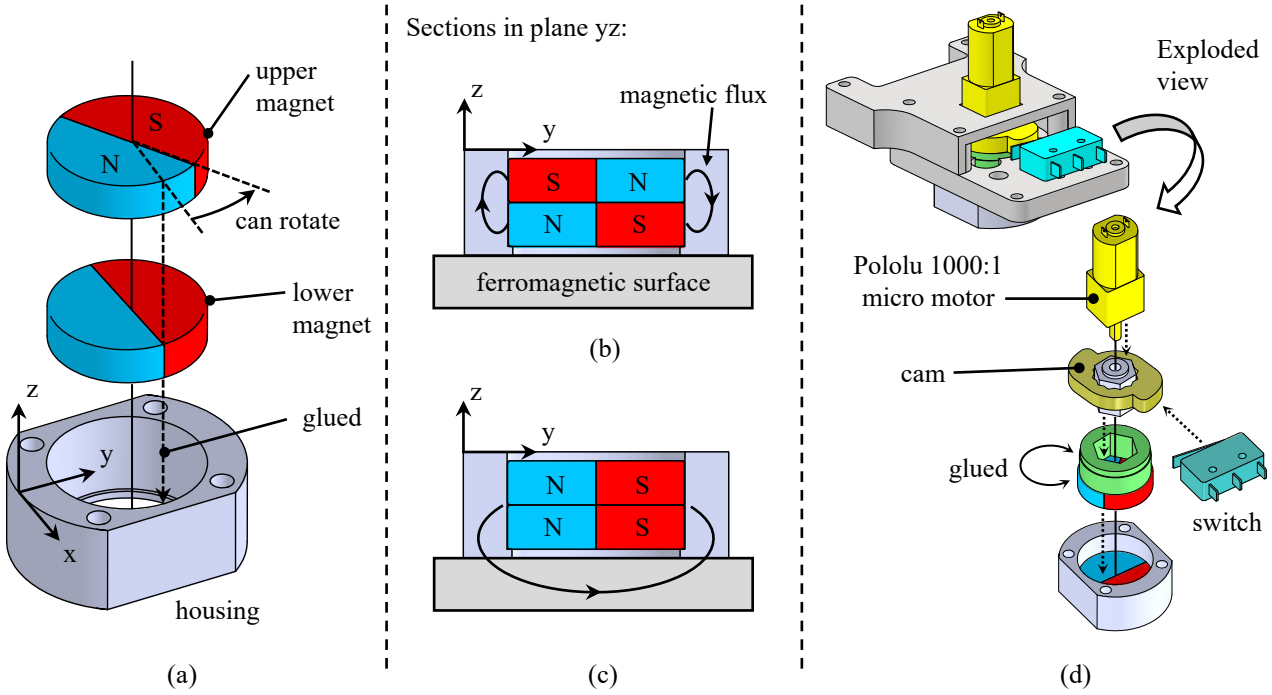

Figure 13: (a-c) Working principle of switchable permanent magnets. (d) Mechanism for switching magnets of body A.

the surface). Switchable magnets offer many advantages over traditional electromagnets [43], such as higher safety (adhesion will not cease after power failure), lower energy consumption (energy is not required for keeping the adhesion forces, only for turning them ON/OFF), and higher adhesion forces per unit mass.

For example, consider the device illustrated in Figure 13a. It consists of a steel housing containing two cylindrical permanent magnets with diametral magnetization. The lower magnet is rigidly attached to the housing (e.g., through glue). The upper magnet can freely rotate about the common axis of both magnets, and this rotation can be governed by a small motor. When the poles of both magnets are placed antagonistically (Figure 13b), magnetic flux flows internally through the housing from each North to the South of the other magnet, not providing magnetic adhesion to an external ferromagnetic surface. However, after the upper magnet is rotated by 180°, the North poles of both magnets become aligned, and magnetic flux flows mainly through the external surface to the South poles, providing adhesion to the surface (Figure 13c). This is not the only way to arrange permanent magnets to generate switchable magnetic devices, there are many other layouts and designs, see Ref. [44] for more examples.

The switchable magnets used in the Xrobin robot are of the type illustrated in Figure 13a. Each body (A or B) has two switchable magnets, as indicated in Figure 12. These magnets are made of the same materials as those used in the HyReCRo biped climbing robot [42], but with slightly different geometry (the housings in [42] have lateral notches that decrease leakages of magnetic flux and increase adhesion forces, which were not necessary for the Xrobin robot). The adhesion force of each individual switchable magnet of the Xrobin robot is about 100N when adhered to 3mm-thick steel plates.

Finally, the ON/OFF switching of these magnets is produced differently in bodies A and B. In body A, each magnet is switched by a Pololu micro motor (12 Vdc and gear ratio 1000:1) which rotates until a 180° rotation is detected by a switch pressed by a cam (see Figure 13d). In body B, this solution was not possible due to the lack of free space above the magnets, since placing Pololu motors on body B would interfere with the motion of linear actuator l (see side view in Figure 11). Alternatively, this problem was solved in body B by placing an additional linear actuator at the bottom of body B, as shown in Figure 12b. As detailed in Figure 14, a rack-and-pinion mechanism is used for transforming the linear motion of this actuator into the 180° rotation of both magnets.

6.2. Electronics and Control

The developed robot carries a custom-made electronic plate, mounted on one of the ends of body A. This plate has an Arduino MKR Wifi 1010 board that controls the robot, as well as amplifying electronics and a relay to activate the rotation of the motors that switch the adhesion state of the magnets of body A. All actuators are commanded from this Arduino board, by applying +12 Vdc or -12 Vdc as required. Power is supplied through wires, which will be replaced by a battery in the

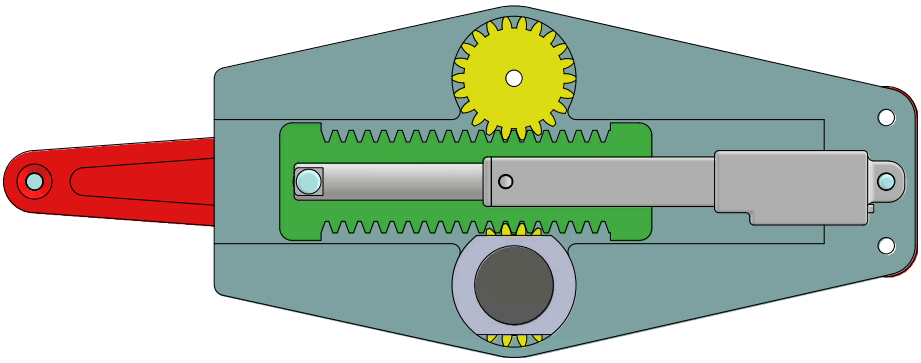

Figure 14: Rack-and-pinion mechanism for switching the adhesion state of the magnets of body B.

future to make the robot completely autonomous. Through a web server, it is possible to command the Arduino wirelessly to completely extend or retract each linear actuator or switch the magnets of body A, in addition to the following commands:

- **Change sign of y:** this command performs a closed trajectory in the plane (l, r) of the 2R$\underline{\text{P}}$R-PR mechanism, in order to switch between the two crossed solutions that this mechanism can adopt for a given state of the inputs (l, r), as explained in Section 3.1. For example, if the robot starts with both actuators completely extended (point 11 of Figure 3a) and assembled with positive crossed solution (point X_{11}^{+} of Figure 3b), clicking this option will perform the closed trajectory $11 \rightarrow 10 \rightarrow 00 \rightarrow 01 \rightarrow 11$ in plane (l, r), which generates the trajectory $X_{11}^{+} \rightarrow X_{10}^{+} \rightarrow X_{00}^{+} \rightarrow X_{01}^{-} \rightarrow X_{11}^{-}$ in plane (ϕ, y). The overall effect of this trajectory is to change the signs of y and ϕ.

- **Move forward:** this command performs the next sequence of operations, assuming that the robot starts with the solution X_{11}^{+}, which is the one shown in Figure 11, with body B attached to the plane of motion and body A detached from it:

  1. Execute the "*Change sign of y*" command explained above, to travel from solution X_{11}^{+} to solution X_{11}^{-}.
  2. Attach body A to the plane of motion. After this, detach body B from it.
  3. Execute again the "*Change sign of y*" command, to return to the original solution X_{11}^{+}.

  The overall effect of this sequence is that body A moves forward by a theoretical distance of $2 \cdot y_0 = 100.48$mm, preserving its orientation. A similar command moves the robot backward by the same distance.

- **Turn right:** this command performs the following operations to rotate the robot clockwise by 90°, assuming that the robot starts with the X_{11}^{+} solution, with body A initially attached to the plane of motion and body B detached from it:

  1. Retract actuator l ($X_{11}^{+} \rightarrow X_{01}^{+}$). After this, retract actuator r ($X_{01}^{+} \rightarrow X_{00}^{-}$).
  2. Attach body B. After this, release body A.
  3. Extend actuator r ($X_{00}^{-} \rightarrow X_{01}^{+}$). After this, extend actuator l ($X_{01}^{+} \rightarrow X_{11}^{+}$).

  The overall effect of this sequence is a clockwise rotation of the whole robot by 90°, accompanied by a translation of its center about $y_0 = 50.24$mm to the left of the starting position (this motion corresponds to the leftmost point of the workspace shown in Figure 7a). A similar command turns the robot 90° to the left.

6.3. Experiments

This section shows three experiments performed with the prototype described in the preceding paragraphs. A photo of the actual prototype is shown in Figure 15. The constructive parts of bodies A and B are made of 3D-printed PLA, whereas all other elements have been described above. The robot weighs 0.75kg.

Next, three experiments are presented, in order to illustrate some of the commands explained in the previous section. These experiments were performed on a 3mm-thick horizontal steel plate. A video recording of these experiments is attached to the paper as a supplementary material, in order to see the robot in motion. The three experiments were conducted in a row.

The first experiment is illustrated in Figure 16. During this experiment, body A is attached to the steel plate and body B is free. The initial configuration of the robot is X_{11}^{+} (Figure 16a). The objective of this experiment is to demonstrate that the prototype can visit all eight solutions $X_{ij}^{\pm}$ illustrated in Figures 3b and 4, avoiding mechanical collisions between its parts. To this end, the "*Change sign of y*" command explained in Section 6.2 is executed once to travel from solution X_{11}^{+} to solution X_{11}^{-} (sequence: Figure 16a-b-c-d-e). Then, the same command is executed once again to return to solution X_{11}^{+} from solution X_{11}^{-}

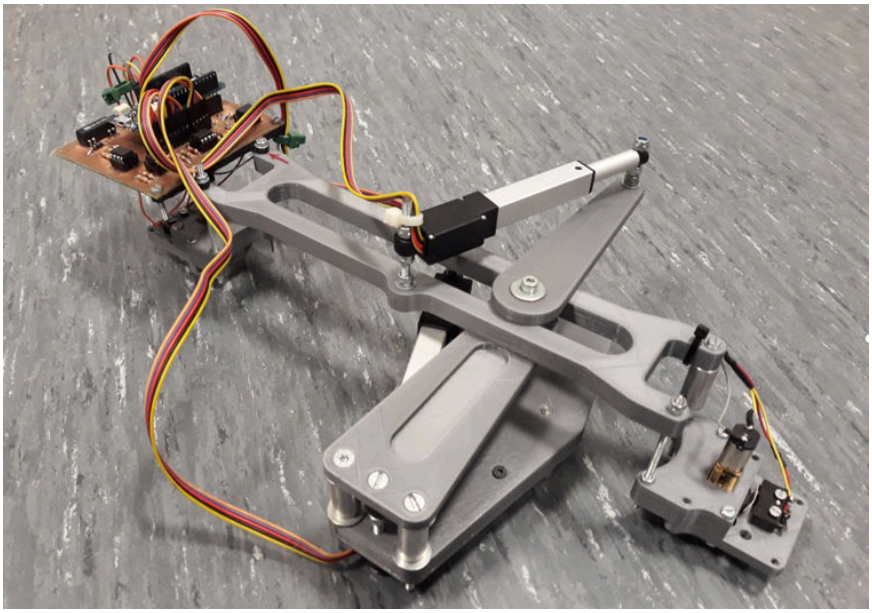

Figure 15: Photo of the built prototype.

(sequence: Figure 16e-f-g-h-a). Thus, in this experiment the robot performs a clockwise closed trajectory around the origin of plane (ϕ, y), which starts and ends at X_{11}^{+}, after visiting all eight solutions.

The second experiment is illustrated in Figure 17. This Figure should be interpreted by following the arrows drawn on it, starting from the "Start" label in Figure 17a, and ending at the "End" label of Figure 17i. The starting point of this experiment is where the previous experiment finished: the robot is assembled with solution X_{11}^{+}, with body A attached to the steel plate and body B free. To begin this second experiment, body B is attached first to the steel plate. After this, body A is detached from it. Then, the "*Move forward*" command is executed, performing the sequence of operations explained in Section 6.2. As a result of this command, the robot performs the motions illustrated in the sequence of Figure 17a-b-c-d-e-f-g-h-i. Comparing Figure 17i with Figure 17j (which is a repetition of Figure 17a) by drawing horizontal dashed lines across both figures, it is observed that the overall effect of this sequence is a pure forward translation of the robot, by a distance $\Delta y \approx 93$ mm. Ideally, this distance should be $2 \cdot y_0 = 100.48$mm, but this difference can be reduced by decreasing joint clearances, friction, and manufacturing tolerances. Similarly, a vertical dashed line has been drawn across Figures 17a and 17i, so that the initial and final poses can also be compared vertically. This vertical comparison shows that the robot does not rotate or translate horizontally appreciably, which confirms that the overall motion is a pure forward translation.

Finally, the third experiment is illustrated in Figure 18. Starting where the second experiment ended, with solution X_{11}^{+}, with body A attached to the steel plate and body B free, the "*Turn right*" command is executed, performing the motions explained in Section 6.2. The result of these motions is shown in the sequence of Figures 18a-b-c-d-e. To assess the overall effect of this sequence, a reference frame Σ_A has been drawn on the initial and final poses of Figures 18a and 18e. This frame is rigidly attached to the center of body A, as in Figure 2a (with axis Y directed along the slot). Figures 18a and 18e are overlapped in Figure 18f using transparency. As Figure 18f shows, the overall effect of this turning command is a $-90°$ rotation of the robot plus a slight translation to the left.

7. Conclusions and Future Work

In this paper, we have presented Xrobin, a binary-actuated sliding-frame mobile robot based on a 2RPR-PR parallel mechanism with crossed (X) actuators. The robot has two bodies connected by a pin-in-slot joint and two linear actuators, and it moves by alternately attaching one body or the other to the plane of motion, while extending the linear actuators to move the free body. The main novelty of this mobile robot is that it can adopt eight different configurations using only two binary actuators, instead of reaching only four configurations like ordinary robots driven by two binary actuators. This is possible thanks to the ability of the 2RPR-PR mechanism to perform nonsingular transitions between different configurations that correspond to the same state of the actuators. We have addressed the design problem of the robot by solving its kinematic equations for prescribed poses and actuator strokes, and analyzed the workspace of the designed robot, demonstrating that it has a very dense workspace that allows it to reach nearby points with high accuracy and with any orientation multiple of 45°. Comparisons with an alternative version of the parallel robot with non-crossed actuators lacking the ability to perform

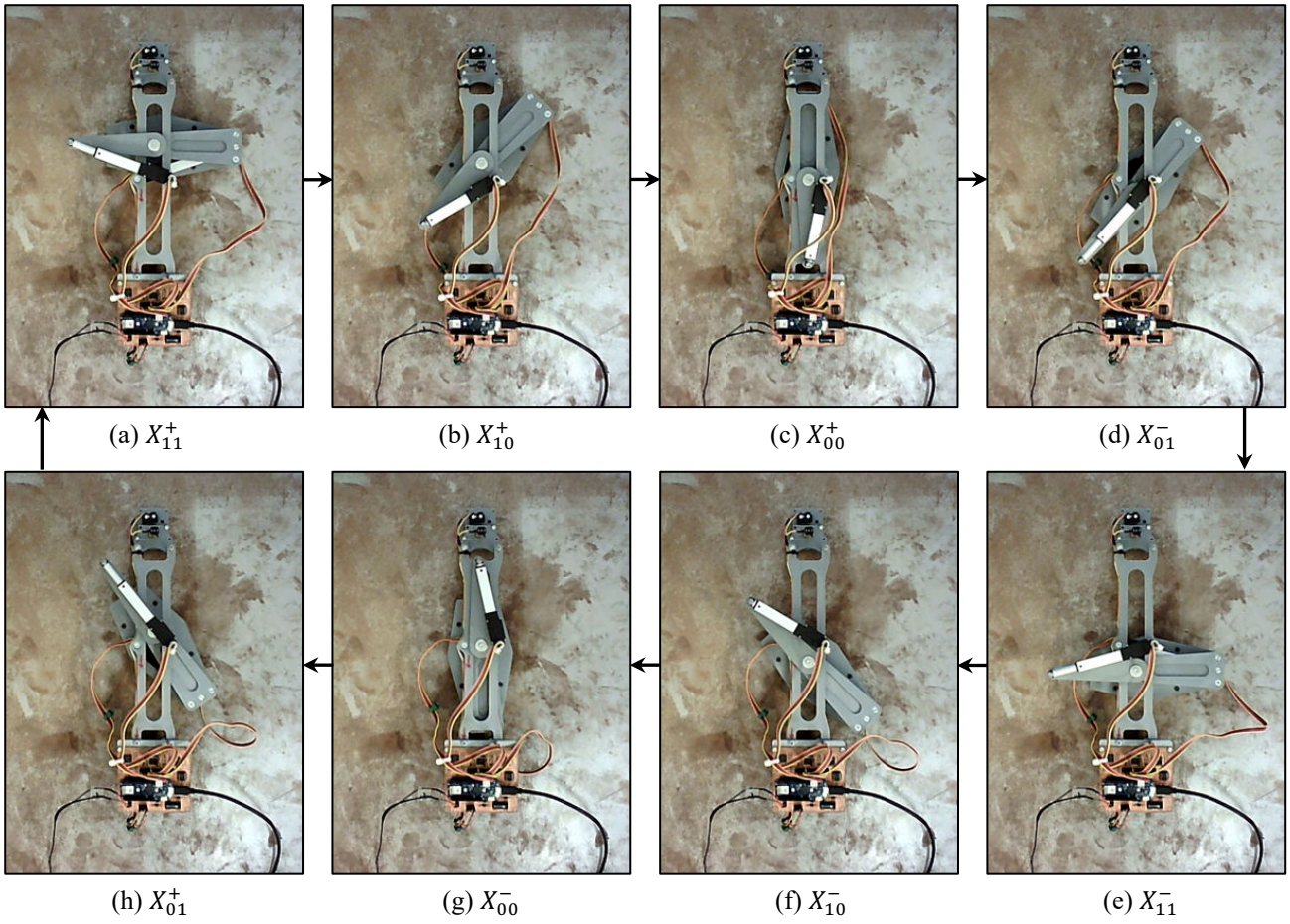

Figure 16: Robot visiting all eight configurations that can be reached by using two binary actuators. Note that Figure 4 is a simulated version of this figure.

nonsingular transitions, and with a traditional equivalent serially-actuated robot, have revealed that assembling the robot with crossed actuators yields a larger, denser, and more symmetric and uniform workspace, which reinforces the advantages of exploiting the nonsingular transitions of parallel mechanisms. Finally, the designed robot has been materialized in the form of a functional prototype, whose implementation has been described in detail, with experiments demonstrating that the robot can reach all desired configurations and move as expected, avoiding self-collisions between different moving parts.

To conclude, regarding possible continuations of the presented work, in the future we will substitute the wired power supply of the robot by a battery, to make it more autonomous. Also, a camera will be mounted on the robot to perform autonomous visual inspection of its environment, as well as localization and mapping. Finally, the trajectory planning problem of the robot will be solved, to determine the optimal sequence of movements necessary to reach some desired position and orientation with prescribed accuracy, subject to the discrete yet highly dense workspace of the proposed robot.

Funding

This work was supported by the Spanish Ministry of Science and Innovation [grant number: PID2020-116418RB-I00, "HYREBOT: Robots híbridos y reconstrucción multisensorial para aplicaciones en estructuras reticulares"].

References

[1] D. Schmidt, K. Berns, Climbing robots for maintenance and inspections of vertical structures - A survey of design aspects and technologies, Robotics and Autonomous Systems 61 (12) (2013) 1288–1305. doi:10.1016/j.robot.2013.09.002.

[2] J. Shang, T. Sattar, S. Chen, B. Bridge, Design of a climbing robot for inspecting aircraft wings and fuselage, Industrial Robot: An International Journal 34 (6) (2007) 495–502. doi:https://doi.org/10.1108/01439910710832093.

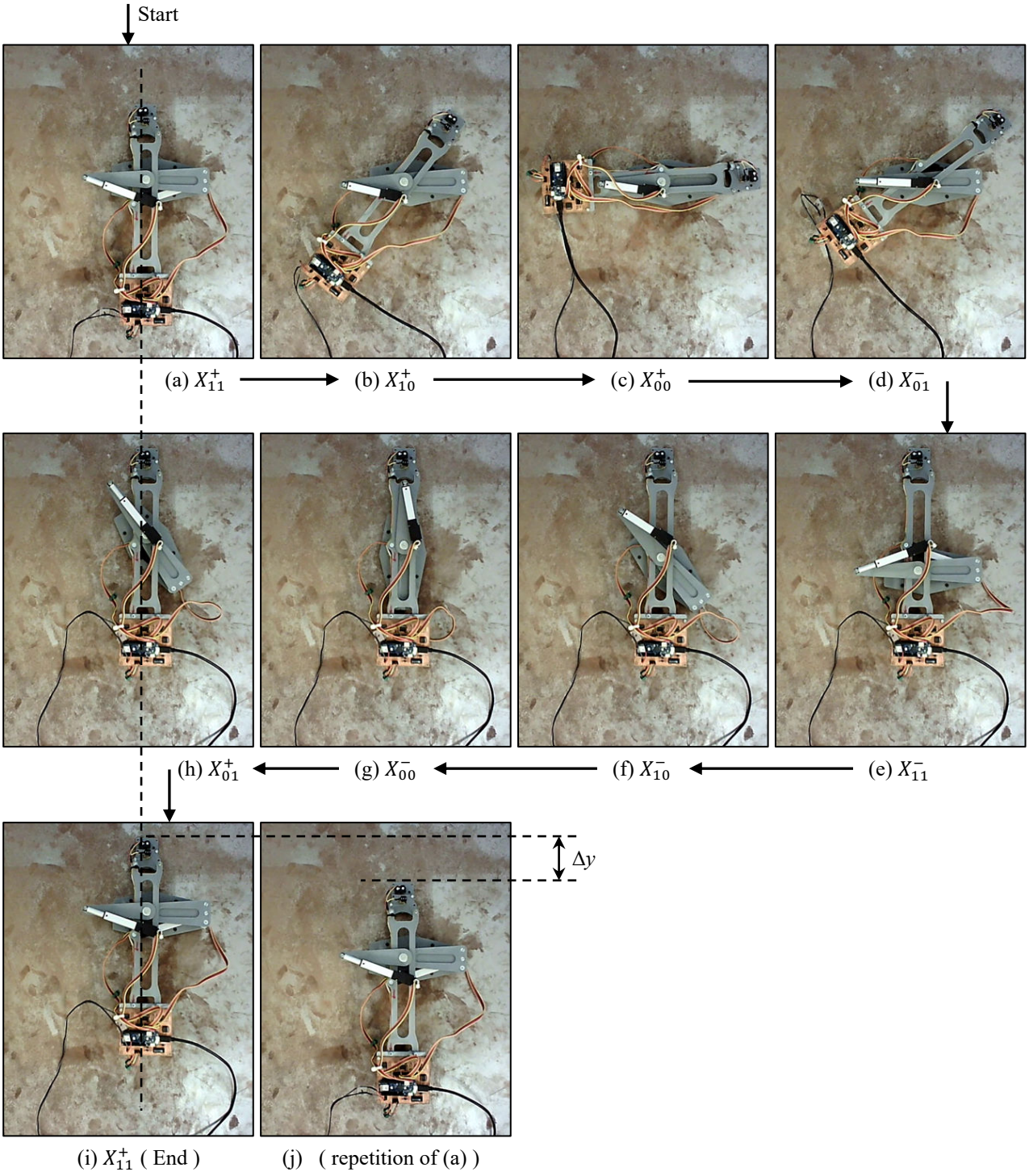

Figure 17: Robot performing a forward motion.

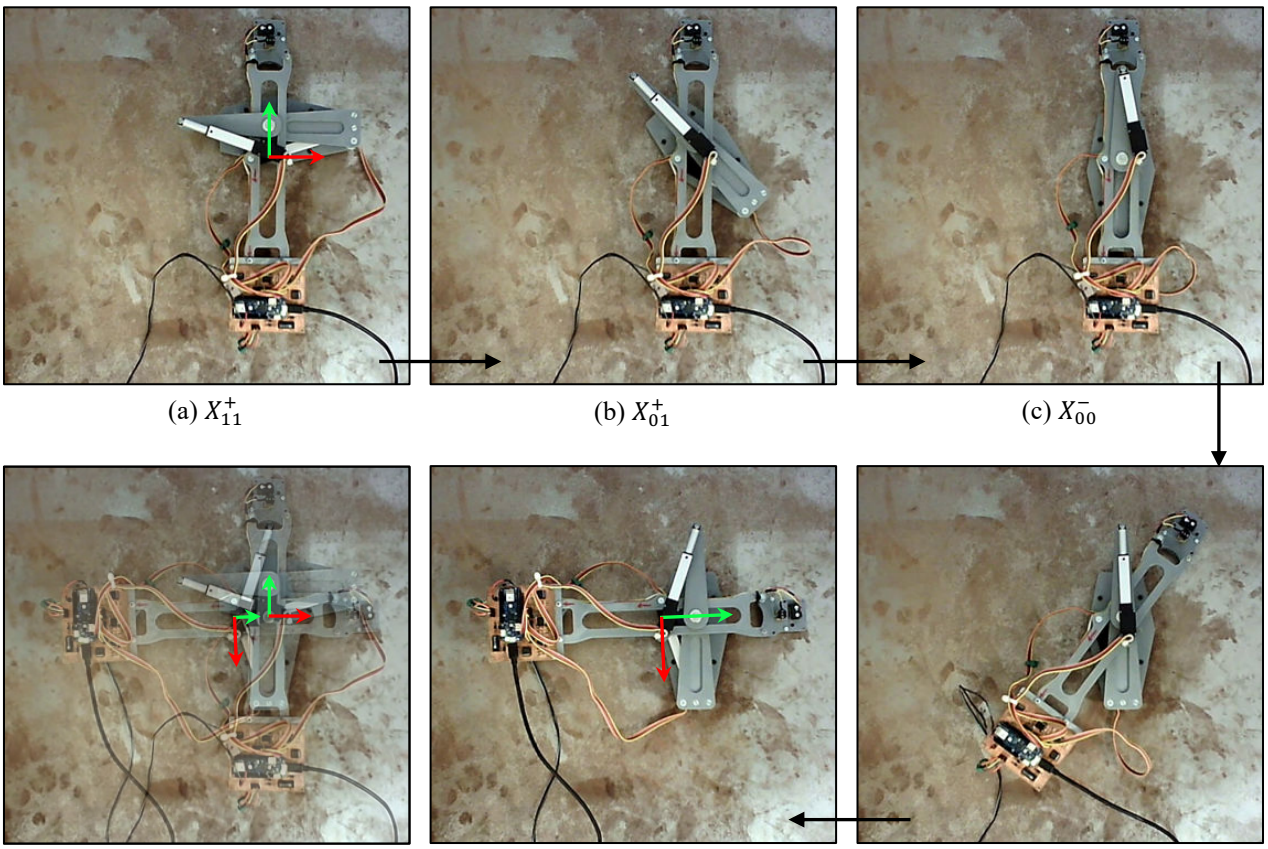

Figure 18: Robot performing a turn-right motion.

[3] H. Zhang, J. Zhang, G. Zong, W. Wang, R. Liu, Sky Cleaner 3: A real pneumatic climbing robot for glass-wall cleaning, IEEE Robotics & Automation Magazine 13 (1) (2006) 32–41. doi:10.1109/MRA.2006.1598051.

[4] H. Zhang, W. Wang, J. Zhang, High stiffness pneumatic actuating scheme and improved position control strategy realization of a pneumatic climbing robot, in: 2008 IEEE International Conference on Robotics and Biomimetics, IEEE, 2009, pp. 1806–1811. doi:10.1109/ROBIO.2009.4913276.

[5] H. Zhang, J. Zhang, R. Liu, G. Zong, Realization of a service robot for cleaning spherical surfaces, International Journal of Advanced Robotic Systems 2 (1) (2005) 53–58. doi:https://doi.org/10.5772/5800.

[6] P. G. Backes, Y. Bar-Cohen, B. Joffe, The multifunction automated crawling system (MACS), in: Proceedings of International Conference on Robotics and Automation, Vol. 1, IEEE, 1997, pp. 335–340. doi:10.1109/ROBOT.1997.620060.

[7] B. Luk, T. White, D. Cooke, N. Hewer, G. Hazel, S. Chen, Climbing service robot for duct inspection and maintenance applications in a nuclear reactor, in: Proceedings of the 32nd ISR (International Symposium on Robotics), 2001, pp. 41–46.

[8] B. Luk, A. Collie, D. Cooke, S. Chen, Walking and climbing service robots for safety inspection of nuclear reactor pressure vessels, Measurement and control 39 (2) (2006) 43–47. doi:https://doi.org/10.1177/002029400603900201.

[9] G. La Rosa, M. Messina, G. Muscato, R. Sinatra, A low-cost lightweight climbing robot for the inspection of vertical surfaces, Mechatronics 12 (1) (2002) 71–96. doi:https://doi.org/10.1016/S0957-4158(00)00046-5.

[10] J. Savall, A. Avello, L. Briones, Two compact robots for remote inspection of hazardous areas in nuclear power plants, in: Proceedings 1999 IEEE International Conference on Robotics and Automation, Vol. 3, IEEE, 1999, pp. 1993–1998. doi:10.1109/ROBOT.1999.770400.

[11] T. Apostolescu, C. Udrea, D. Duminica, G. Ionascu, L. Bogatu, L. A. Cartal, Development of a climbing robot with vacuum attachment cups, The Romanian Review Precision Mechanics 40 (2011) 92–97.

[12] C. L. Wolfe, M. Siegel, C. J. Alberts, W. M. Kaufman, Robot with cruciform geometry (U.S. Patent 5429009, Jul. 4, 1995).

[13] D. Souto, A. Faiña, A. Deibe, F. Lopez-Peña, R. J. Duro, A robot for the unsupervised grit-blasting of ship hulls, International Journal of Advanced Robotic Systems 9 (3) (2012) 82. doi:https://doi.org/10.5772/50847.

[14] I.-M. Chen, S. H. Yeo, Locomotion of a two-dimensional walking-climbing robot using a closed-loop mechanism: From gait generation to navigation, The International Journal of Robotics Research 22 (1) (2003) 21–40. doi:https://doi.org/10.1177/0278364903022001003.

[15] P. Dutkiewicz, K. Kozłowski, W. Wróblewski, Inspection robot SAFARI–construction and control, Bulletin of the Polish Academy of Sciences: Technical Sciences 52 (2) (2004) 119–129.

[16] A. Peidró, J. María Marín, A. Gil, Ó. Reinoso, Performing nonsingular transitions between assembly modes in analytic parallel manipulators by enclosing quadruple solutions, Journal of Mechanical Design 137 (12) (2015) 122302. doi:10.1115/1.4031653.

[17] M. Urízar, V. Petuya, O. Altuzarra, M. Diez, A. Hernández, Non-singular transitions based design methodology for parallel manipulators, Mechanism and Machine Theory 91 (2015) 168–186. doi:https://doi.org/10.1016/j.mechmachtheory.2015.04.010.

[18] D. Schütz, A. Raatz, J. Hesselbach, The development of a reconfigurable parallel robot with binary actuators, in: Advances in Robot Kinematics: Motion in Man and Machine, Springer, 2010, pp. 225–232. doi:10.1007/978-90-481-9262-5_24.

[19] A. Bayram, M. Kemal Özgören, The conceptual design of a spatial binary hyper redundant manipulator and its forward kinematics, Proceedings of the Institution of Mechanical Engineers, Part C: Journal of Mechanical Engineering Science 226 (1) (2012) 217–227. doi:10.1177/0954406211412156.

[20] K. Maeda, E. Konaka, Inverse kinematics solution algorithm for continuous/binary hybrid manipulator, in: 2015 IEEE International Conference on Automation Science and Engineering (CASE), IEEE, 2015, pp. 483–488. doi:10.1109/CoASE.2015.7294126.

[21] I. Ebert-uphoff, G. S. Chirikjian, Efficient workspace generation for binary manipulators with many actuators, Journal of Robotic Systems 12 (6) (1995) 383–400. doi:10.1002/rob.4620120605.

[22] D. S. Lees, G. S. Chirikjian, An efficient method for computing the forward kinematics of binary manipulators, in: Proceedings of IEEE International Conference on Robotics and Automation, Vol. 2, IEEE, 1996, pp. 1012–1017. doi:10.1109/ROBOT.1996.506841.

[23] G. S. Chirikjian, Inverse kinematics of binary manipulators using a continuum model, Journal of Intelligent and Robotic Systems 19 (1) (1997) 5–22. doi:10.1023/A:1007942530293.

[24] R. Clysdale, Q. Sun, Motion planning for planar binary robots in a reduced workspace, in: IEEE 2005 International Conference Mechatronics and Automation, Vol. 1, IEEE, 2005, pp. 388–393. doi:10.1109/ICMA.2005.1626578.

[25] J. Suthakorn, G. S. Chirikjian, Design and implementation of a new discretely-actuated manipulator, in: D. Rus, S. Singh (Eds.), Experimental Robotics VII, Springer, Berlin, Heidelberg, 2001, pp. 151–157. doi:10.1007/3-540-45118-8_16.

[26] K. Maeda, E. Konaka, Ellipsoidal outer-approximation of workspace of binary manipulator for inverse kinematics solution, in: 2014 IEEE/ASME International Conference on Advanced Intelligent Mechatronics, IEEE, 2014, pp. 1331–1336. doi:10.1109/AIM.2014.6878267.

[27] E. Tzorakoleftherakis, A. Mavrommati, A. Tzes, Design and implementation of a binary redundant manipulator with cascaded modules, Journal of Mechanisms and Robotics 8 (1) (2016) 011002. doi:10.1115/1.4030372.

[28] V. A. Sujan, S. Dubowsky, Design of a lightweight hyper-redundant deployable binary manipulator, Journal of Mechanical Design 126 (1) (2004) 29–39. doi:10.1115/1.1637647.

[29] Y. Miao, F. Gao, Y. Zhang, Gait fitting for snake robots with binary actuators, Science China Technological Sciences 57 (1) (2014) 181–191. doi:10.1007/s11431-013-5405-0.

[30] D. Úbeda, J. M. Marín, A. Gil, O. Reinoso, Design and postures of a serial robot composed by closed-loop kinematics chains, in: S. Kucuk (Ed.), Serial and Parallel Robot Manipulators - Kinematics, Dynamics, Control and Optimization, IntechOpen, Rijeka, 2012, Ch. 7, pp. 125–142. doi:10.5772/33364.

[31] E. Ottaviano, M. Ceccarelli, J. D. Giorgio, M. Varone, Design and evaluation of a discretely actuated multi-module parallel manipulator, Proceedings of the Institution of Mechanical Engineers, Part C: Journal of Mechanical Engineering Science 220 (4) (2006) 513–526. doi:10.1243/09544062C08305.

[32] S. Tappe, J. Pohlmann, J. Kotlarski, T. Ortmaier, Optimization strategies for task specific path-following capabilities of a binary actuated snake-like robot using follow-the-leader control, in: 2017 IEEE International Conference on Advanced Intelligent Mechatronics (AIM), IEEE, 2017, pp. 1574–1581. doi:10.1109/AIM.2017.8014243.

[33] K. Tadakuma, L. M. DeVita, J.-S. Plante, Y. Shaoze, S. Dubowsky, The experimental study of a precision parallel manipulator with binary actuation: With application to MRI cancer treatment, in: 2008 IEEE International Conference on Robotics and Automation, IEEE, 2008, pp. 2503–2508. doi:10.1109/ROBOT.2008.4543589.

[34] S. J. Lee, A. M. Bilton, S. Dubowsky, On the kinematics of solar mirrors using massively parallel binary actuation, in: Proceedings of the ASME 2010 International Design Engineering Technical Conferences and Computers and Information in Engineering Conference, Vol. 2: 34th Annual Mechanisms and Robotics Conference, Parts A and B, 2010, pp. 1177–1186. doi:10.1115/DETC2010-28875.

[35] W. Ding, Y.-A. Yao, Construction and locomotion analysis of modular robots with pneumatic-actuated and binary-controlled expandable cubes, Advanced Robotics 28 (22) (2014) 1487–1505. doi:10.1080/01691864.2014.959052.

[36] R. Liu, Y.-A. Yao, W. Ding, X.-P. Liu, Locomotion optimization and manipulation planning of a tetrahedron-based mobile mechanism with binary control, Chinese Journal of Mechanical Engineering 31 (1) (2018) 1–22. doi:10.1186/s10033-018-0215-8.

[37] D. Schütz, A. Raatz, J. Hesselbach, Adapted task configuration of a reconfigurable binary parallel robot with PRRRP structure, Robotica 31 (2) (2013) 285–293. doi:10.1017/S0263574712000240.

[38] Y. Zhou, On the planar stability of rigid-link binary walking robots, Robotica 21 (6) (2003) 667–675. doi:10.1017/S0263574703005162.

[39] A. Peidró, A. Gil, J. M. Marín, Y. Berenguer, O. Reinoso, Kinematic analysis and simulation of a hybrid biped climbing robot, in: Proceedings of the 12th International Conference on Informatics in Control, Automation and Robotics (ICINCO), Vol. 2, IEEE, 2015, pp. 24–34. doi:10.5220/0005515800240034.

[40] M. Coste, P. Wenger, D. Chablat, Hidden cusps, in: J. Lenarčič, J.-P. Merlet (Eds.), Advances in Robot Kinematics 2016, Springer International Publishing, Cham, 2018, pp. 129–138. doi:10.1007/978-3-319-56802-7_14.

[41] E. J. Haug, Computer-Aided Kinematics and Dynamics of Mechanical Systems, Volume II: Modern Methods, 2nd Ed., ResearchGate, Berlin, 2021.

[42] A. Peidró, M. Tavakoli, J. M. Marín, O. Reinoso, Design of compact switchable magnetic grippers for the HyReCRo structure-climbing robot, Mechatronics 59 (2019) 199–212. doi:10.1016/j.mechatronics.2019.04.007.

[43] M. Tavakoli, C. Viegas, J. C. Romão, P. Neto, A. T. de Almeida, Switchable magnets for robotics applications, in: 2015 IEEE/RSJ International Conference on Intelligent Robots and Systems (IROS), 2015, pp. 4325–4330. doi:10.1109/IROS.2015.7353990.

[44] F. Rochat, P. Schoeneich, M. Bonani, S. Magnenat, F. Mondada, H. Bleuler, C. Hürzeler, Design of magnetic switchable device (MSD) and applications in climbing robot, in: Emerging Trends in Mobile Robotics, World Scientific, 2010, pp. 375–382. doi:10.1142/9789814329927_0047.